Synthesis of Novel Integrated Actuators Powered by Shape Memory Alloys

THIS IS A TEMPORARY TITLE PAGE
It will be replaced for the final print by a version
provided by the registrar's office.

Thèse n. 1234 2021
présentée le 17 juin 2021
à la Faculté des sciences de base
Integrated Actuators Laboratory
Programme Doctoral en Robotics, Control, and Intelligent Systems
École polytechnique fédérale de Lausanne

pour l'obtention du grade de Docteur ès Sciences
par

Sean Thomas

acceptée sur proposition du jury :

Prof Name Surname, président du jury
Prof Name Surname, directeur de thèse
Prof Name Surname, rapporteur
Prof Name Surname, rapporteur
Prof Name Surname, rapporteur

Lausanne, EPFL, 2021

Wings are a constraint that makes
it possible to fly.
— Robert Bringhurst

To my parents. . .

Acknowledgements

Lorem ipsum dolor sit amet, consectetuer adipiscing elit. Ut purus elit, vestibulum ut, placerat ac, adipiscing vitae, felis. Curabitur dictum gravida mauris. Nam arcu libero, nonummy eget, consectetuer id, vulputate a, magna. Donec vehicula augue eu neque. Pellentesque habitant morbi tristique senectus et netus et malesuada fames ac turpis egestas. Mauris ut leo. Cras viverra metus rhoncus sem. Nulla et lectus vestibulum urna fringilla ultrices. Phasellus eu tellus sit amet tortor gravida placerat. Integer sapien est, iaculis in, pretium quis, viverra ac, nunc. Praesent eget sem vel leo ultrices bibendum. Aenean faucibus. Morbi dolor nulla, malesuada eu, pulvinar at, mollis ac, nulla. Curabitur auctor semper nulla. Donec varius orci eget risus. Duis nibh mi, congue eu, accumsan eleifend, sagittis quis, diam. Duis eget orci sit amet orci dignissim rutrum.

Nam dui ligula, fringilla a, euismod sodales, sollicitudin vel, wisi. Morbi auctor lorem non justo. Nam lacus libero, pretium at, lobortis vitae, ultricies et, tellus. Donec aliquet, tortor sed accumsan bibendum, erat ligula aliquet magna, vitae ornare odio metus a mi. Morbi ac orci et nisl hendrerit mollis. Suspendisse ut massa. Cras nec ante. Pellentesque a nulla. Cum sociis natoque penatibus et magnis dis parturient montes, nascetur ridiculus mus. Aliquam tincidunt urna. Nulla ullamcorper vestibulum turpis. Pellentesque cursus luctus mauris.

Lausanne, June 17, 2021 D. K.

Preface

A preface is not mandatory. It would typically be written by some other person (eg your thesis director).

Lorem ipsum dolor sit amet, consectetuer adipiscing elit. Ut purus elit, vestibulum ut, placerat ac, adipiscing vitae, felis. Curabitur dictum gravida mauris. Nam arcu libero, nonummy eget, consectetuer id, vulputate a, magna. Donec vehicula augue eu neque. Pellentesque habitant morbi tristique senectus et netus et malesuada fames ac turpis egestas. Mauris ut leo. Cras viverra metus rhoncus sem. Nulla et lectus vestibulum urna fringilla ultrices. Phasellus eu tellus sit amet tortor gravida placerat. Integer sapien est, iaculis in, pretium quis, viverra ac, nunc. Praesent eget sem vel leo ultrices bibendum. Aenean faucibus. Morbi dolor nulla, malesuada eu, pulvinar at, mollis ac, nulla. Curabitur auctor semper nulla. Donec varius orci eget risus. Duis nibh mi, congue eu, accumsan eleifend, sagittis quis, diam. Duis eget orci sit amet orci dignissim rutrum.

Nam dui ligula, fringilla a, euismod sodales, sollicitudin vel, wisi. Morbi auctor lorem non justo. Nam lacus libero, pretium at, lobortis vitae, ultricies et, tellus. Donec aliquet, tortor sed accumsan bibendum, erat ligula aliquet magna, vitae ornare odio metus a mi. Morbi ac orci et nisl hendrerit mollis. Suspendisse ut massa. Cras nec ante. Pellentesque a nulla. Cum sociis natoque penatibus et magnis dis parturient montes, nascetur ridiculus mus. Aliquam tincidunt urna. Nulla ullamcorper vestibulum turpis. Pellentesque cursus luctus mauris.

Lausanne, 12 Mars 2011 T. D.

Abstract

Lorem ipsum dolor sit amet, consectetuer adipiscing elit. Ut purus elit, vestibulum ut, placerat ac, adipiscing vitae, felis. Curabitur dictum gravida mauris. Nam arcu libero, nonummy eget, consectetuer id, vulputate a, magna. Donec vehicula augue eu neque. Pellentesque habitant morbi tristique senectus et netus et malesuada fames ac turpis egestas. Mauris ut leo. Cras viverra metus rhoncus sem. Nulla et lectus vestibulum urna fringilla ultrices. Phasellus eu tellus sit amet tortor gravida placerat. Integer sapien est, iaculis in, pretium quis, viverra ac, nunc. Praesent eget sem vel leo ultrices bibendum. Aenean faucibus. Morbi dolor nulla, malesuada eu, pulvinar at, mollis ac, nulla. Curabitur auctor semper nulla. Donec varius orci eget risus. Duis nibh mi, congue eu, accumsan eleifend, sagittis quis, diam. Duis eget orci sit amet orci dignissim rutrum.

Nam dui ligula, fringilla a, euismod sodales, sollicitudin vel, wisi. Morbi auctor lorem non justo. Nam lacus libero, pretium at, lobortis vitae, ultricies et, tellus. Donec aliquet, tortor sed accumsan bibendum, erat ligula aliquet magna, vitae ornare odio metus a mi. Morbi ac orci et nisl hendrerit mollis. Suspendisse ut massa. Cras nec ante. Pellentesque a nulla. Cum sociis natoque penatibus et magnis dis parturient montes, nascetur ridiculus mus. Aliquam tincidunt urna. Nulla ullamcorper vestibulum turpis. Pellentesque cursus luctus mauris.

Zusammenfassung

Lorem ipsum dolor sit amet, consectetuer adipiscing elit. Ut purus elit, vestibulum ut, placerat ac, adipiscing vitae, felis. Curabitur dictum gravida mauris. Nam arcu libero, nonummy eget, consectetuer id, vulputate a, magna. Donec vehicula augue eu neque. Pellentesque habitant morbi tristique senectus et netus et malesuada fames ac turpis egestas. Mauris ut leo. Cras viverra metus rhoncus sem. Nulla et lectus vestibulum urna fringilla ultrices. Phasellus eu tellus sit amet tortor gravida placerat. Integer sapien est, iaculis in, pretium quis, viverra ac, nunc. Praesent eget sem vel leo ultrices bibendum. Aenean faucibus. Morbi dolor nulla, malesuada eu, pulvinar at, mollis ac, nulla. Curabitur auctor semper nulla. Donec varius orci eget risus. Duis nibh mi, congue eu, accumsan eleifend, sagittis quis, diam. Duis eget orci sit amet orci dignissim rutrum.

Nam dui ligula, fringilla a, euismod sodales, sollicitudin vel, wisi. Morbi auctor lorem non justo. Nam lacus libero, pretium at, lobortis vitae, ultricies et, tellus. Donec aliquet, tortor sed accumsan bibendum, erat ligula aliquet magna, vitae ornare odio metus a mi. Morbi ac orci et nisl hendrerit mollis. Suspendisse ut massa. Cras nec ante. Pellentesque a nulla. Cum sociis natoque penatibus et magnis dis parturient montes, nascetur ridiculus mus. Aliquam tincidunt urna. Nulla ullamcorper vestibulum turpis. Pellentesque cursus luctus mauris.

Résumé

Lorem ipsum dolor sit amet, consectetuer adipiscing elit. Ut purus elit, vestibulum ut, placerat ac, adipiscing vitae, felis. Curabitur dictum gravida mauris. Nam arcu libero, nonummy eget, consectetuer id, vulputate a, magna. Donec vehicula augue eu neque. Pellentesque habitant morbi tristique senectus et netus et malesuada fames ac turpis egestas. Mauris ut leo. Cras viverra metus rhoncus sem. Nulla et lectus vestibulum urna fringilla ultrices. Phasellus eu tellus sit amet tortor gravida placerat. Integer sapien est, iaculis in, pretium quis, viverra ac, nunc. Praesent eget sem vel leo ultrices bibendum. Aenean faucibus. Morbi dolor nulla, malesuada eu, pulvinar at, mollis ac, nulla. Curabitur auctor semper nulla. Donec varius orci eget risus. Duis nibh mi, congue eu, accumsan eleifend, sagittis quis, diam. Duis eget orci sit amet orci dignissim rutrum.

Nam dui ligula, fringilla a, euismod sodales, sollicitudin vel, wisi. Morbi auctor lorem non justo. Nam lacus libero, pretium at, lobortis vitae, ultricies et, tellus. Donec aliquet, tortor sed accumsan bibendum, erat ligula aliquet magna, vitae ornare odio metus a mi. Morbi ac orci et nisl hendrerit mollis. Suspendisse ut massa. Cras nec ante. Pellentesque a nulla. Cum sociis natoque penatibus et magnis dis parturient montes, nascetur ridiculus mus. Aliquam tincidunt urna. Nulla ullamcorper vestibulum turpis. Pellentesque cursus luctus mauris.

Contents

Introduction

A non-numbered chapter...

Lorem ipsum dolor sit amet, consectetuer adipiscing elit. Ut purus elit, vestibulum ut, placerat ac, adipiscing vitae, felis. Curabitur dictum gravida mauris. Nam arcu libero, nonummy eget, consectetuer id, vulputate a, magna. Donec vehicula augue eu neque. Pellentesque habitant morbi tristique senectus et netus et malesuada fames ac turpis egestas. Mauris ut leo. Cras viverra metus rhoncus sem. Nulla et lectus vestibulum urna fringilla ultrices. Phasellus eu tellus sit amet tortor gravida placerat. Integer sapien est, iaculis in, pretium quis, viverra ac, nunc. Praesent eget sem vel leo ultrices bibendum. Aenean faucibus. Morbi dolor nulla, malesuada eu, pulvinar at, mollis ac, nulla. Curabitur auctor semper nulla. Donec varius orci eget risus. Duis nibh mi, congue eu, accumsan eleifend, sagittis quis, diam. Duis eget orci sit amet orci dignissim rutrum.

1 Overview of SMA Actuator Design

In this chapter, the traditional design methodology of the SMA actuator is presented. Here, the different building blocks and state-of-the-art of various SMA actuators are presented. An in-depth look at the advantages and limitations of the methodology is conducted.

1.1 Introduction

1.2 Traditional SMA Actuator Design

1.3 Building Blocks of SMA Actuator Design

1.4 SMA Powered Robotic Systems

1.5 Summary and Conclusion

2 Predicting the Shape Memory Effect

In this chapter, different modelling strategies, such as finite element modelling and analytical modelling, are presented. Here, the modelling techniques are employed in the context of the traditional SMA actuator design methodology. Furthermore, the bias spring actuator model and a simplified model are presented.

2.1 Introduction

2.2 Analytical Modelling of the SME

2.3 Finite Element Modelling

2.4 Stroke Estimation of SMA Actuators

2.4.1 Mechanical Modelling

2.4.2 Thermal Model

2.5 Simplified SMA Actuator Model

2.6 Summary and Conclusion

3 Sizing Methodology for Integrated SMA Actuators

3.1 Introduction

In the past few decades, there has been a growing need for miniaturisation. Modern devices have come to require actuators that are compact and lightweight. As mentioned previously, since SMAs have been known to show the highest volumetric work density, they have been increasingly used in applications where compactness and low weight are required.

As previously presented in chapter 1, SMA actuators require an active element, a biasing element and a kinematic stage for motion control. These components, usually discrete elements, when combined together create an SMA actuator that can preform a specific reversible work, such as gripping or crawling motionscite. With the objective of miniaturisation, most work has been conducted into rendering these individual components as compact and lightweight as possiblecite. But the fact that these stages are discrete, lowers the overall volumetric work density of the complete actuator. Furthermore, as multiple systems are needed, the actuator also requires various pieces and assembly increasing the complexity and decreasing the compactness.

Recently, there has been a shift in creating novel motion control mechanisms using flexure-based mechanisms. These flexures are multiple compliant elements designed so as to only be compliant in specific degrees of freedom while being rigid in the others. These mechanisms, which can be fabricated using a monolithic piece of material, are lightweight and require virtually no assembly. These flexural stages, when paired with SMAs, have greatly increased the overall work density of the traditional SMA actuatorscite.

These flexure-based mechanisms are still often integrated into the SMA actuators as discrete mechanisms. In this chapter, the concept of integrating the biasing element as a flexural mechanism is explored. In this case, the kinematic stage and the biasing element are combined and are no longer discrete systems within the mechanism. Some research has been shown to take into account flexure mechanisms in SMA actuators but they lack a suitable sizing strategy due to the complexity of the shape memory effect and the nonlinear nature of flexurescite.

Thus, in this chapter, this novel design methodology is presented and analysed using an analytical model.

3.2 Adapted Design Concept

As mentioned previously, most SMA actuators are composed of an active element, a biasing element and a kinematic stage charged with converting the linear output of the actuator into a more complex one. In general, these elements are discrete components ranging from SMA coils, passive biasing springs and the kinematic stage comprised of hinges and linear slides. As presented in fig. 3.1, the design methodology consists of integrating the kinematic stage and the biasing element.

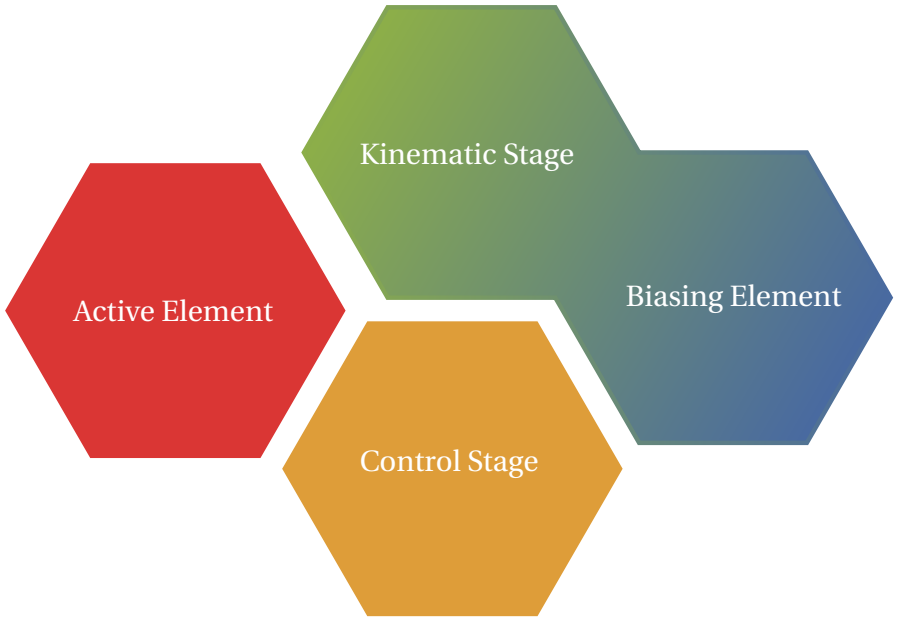

Figure 3.1: Diagram of the adapted building blocks of the SMA actuator.

This integration can be accomplished with the use of flexure-based mechanisms. Generally, flexures have been used in creating an alternative solution for traditional hinges and linear slides. These flexures are comprised of cantilever beams which allows the mechanism to be compliant in a specific degree of freedom while being rigid in the others. The advantages of such a system is that when adequately design can result in a kinematic stage that is lightweight, lacks any assembly and has high precision.

The main drawback to such a system compared to traditional bearings is the inherent stiffness of the mechanism. As these flexures are composed of compliant beams, the rigidity of the beam must be taken into account. In the case of an SMA actuator, this rigidity of the compliant structure can be harnessed as the biasing element. This implies that by pairing the active SMA element with a flexure, the kinematic stage and the biasing element can be combined. This novel approach can be used to create biased SMA actuators that are precise, lightweight and

with a limited number of pieces to be assembled.

3.3 Challenges of the Approach

Due to the complex nature of the shape memory effect, the principle challenge when it comes to designing such SMA actuators is the difficulty in sizing the active SMA based on the flexure mechanism. Based on the configuration of the flexural stage, this mechanism can present highly nonlinear behaviour as well. When paired with an SMA wire or coil, this can results in unintended behaviours or secondary operating points.

Recently there has been research such as the work by Maffiodo et al. (2017) that shows the advantages of pairing SMA wires with flexure-based structures. As with this case, the sizing of the SMA element is disregarding and the biasing advantage of the flexure is neglected.

In the case of grippers and mesoscale actuators where the SMA element is passively cooled, the accurate sizing of the SMA is important. In designs, where passive cooling is used, the geometry of the active element is critical as the shape and structure of the active element is directly related to the cooling times. In the case of SMA coils and wires, thinner diameters imply a shorter cooling time. These thinner wires, however, result in smaller forces when heated. This implies that by accurately sizing the SMA element for the biasing flexure, the actuator can be made as thin as possible while still being able to deform the flexure during heating. Thus, by adapting the traditional sizing methodology of bias-spring SMA actuators for flexure-based designs, the SMA actuator can be designed with faster response times.

3.4 Adapting the Simplified Models

In section 2.5, a simplified model of the SMAs are used to size the active element for bias-spring and antagonistic SMA actuators. In the traditional sizing strategy, a simplified linear model of the SMA and the curve of the spring are used to find the operating points of the actuator which is represented by the intersection of the two curves. This simplification allows a relatively simpler sizing of the components by abstracting the complex nonlinear behaviours of the shape memory effect.

3.4.1 Passive Biasing Compliant Mechanisms

The compliant mechanism, as mentioned previously, acts as the biasing element and as the kinematic stage that produces the desired actuator motion. Here, the basic principle is that the inherent stiffness of the compliant flexure mechanism is harnessed to pre-load the SMA for activation. In this case, at lower temperatures, the SMA is deformed using the energy stored in the compliant mechanism while at higher temperatures, the strain recovered by the shape memory effect is used to deform the compliant mechanism. Based on the design of the

compliant mechanism, the SMA actuator can be made to actuate reversibly in a single degree of freedom while being rigid in the others.

In order to size the actuator and its corresponding passive biasing compliant element, an analytical model can be devised and exploited to predict the various operating points of the final SMA actuator. A pseudo-rigid body model (PSBM) based on the work by Henein (2005) can be used to devise the analytical models of the flexures. The flexure hinges are considered to behave like torsional springs with constant angular stiffness, K_θ. The analytical model can be derived by considering the reaction force exerted by the mechanism on the SMA wire or coil when acting as the biasing element.

While a Newtonian approach is possible, the simplest way to compute the force is to consider the elastic potential energy stored in the flexure hinges as the mechanism deforms. This potential energy stored in one torsional spring as a function of the input displacement of the mechanism, x, as given by :

$$U(x) = \frac{1}{2} K_\theta \left(\theta(x) - \theta_0\right)^2 \tag{3.1}$$

where, in the case of a notch flexure hinge, as shown in fig. 3.2, when rotating by an angle of θ, has a stiffness, as described in Henein (2005), equal to:

$$K_\theta = \frac{2Ebe^{2.5}}{9\pi\sqrt{r}} \tag{3.2}$$

Here, E is the Young modulus of the material, and e,b and r the design parameters of the flexure hinge shown in fig. 3.2.

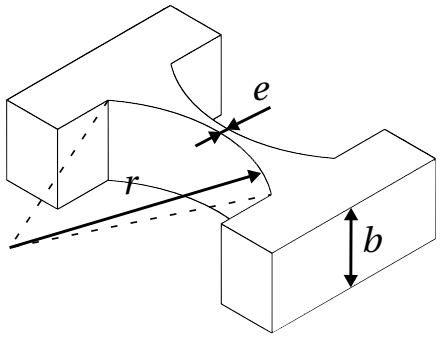

Figure 3.2: A diagram of the notch flexure hinge.

In this approach, the important relationship to obtain is the influence of the contraction of the SMA on the rotation of the hinge, $\theta(x)$. When the flexure-based system is comprised of multiple flexural hinges, the total potential energy can be calculated by the sum of the potential elastic energy of each flexure, $U_{\text{tot}} = \sum U(x)$. The required force to deform the structure can be deduced using :

$$F(\theta(x)) = \|-\nabla U_{\text{tot}}(x)\| = \frac{\partial U_{\text{tot}}(x)}{\partial x} \tag{3.3}$$

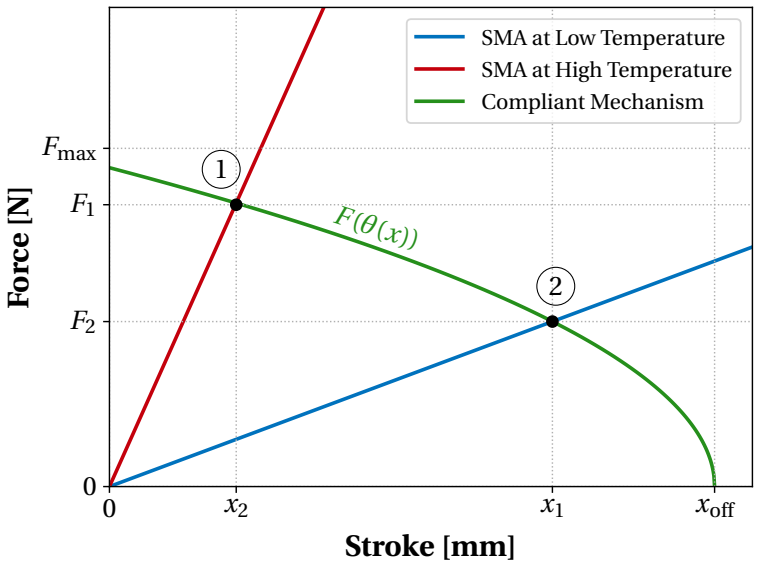

Figure 3.3: The adapted sizing principle of the novel biasing compliant mechanism SMA actuator based on the simplified SMA curves.

As in the case of the traditional SMA sizing methodology, the intersection between the adapted biasing curve and the simplified SMA curves represents the operating points of the SMA actuator, visualised in fig. 3.3 as ① and ②. The stroke of the actuator can be estimated by taking the different between the x-coordinate of the operating points, $\Delta x = x_1 - x_2$. It is important to note that the there is a maximum pull force that the SMA wire or coil can exert, as seen in table cite. Thus, the SMA element must be sized such that $F_1 < F_{max}$ so as to obtain the thinnest SMA wire or coil which can still exert enough force to deform the compliant mechanism to the required stroke.

In fig. 3.4, the design methodology for sizing a biased-compliant mechanism SMA actuator is presented. The methodology consists of designed the SMA active element based on the desired time response (τ) specifications of the application. As explained previously, in the case of passive cooling applications, the wire diameter can be reduced to decrease cooling times and increase τ. Once the diameter of the SMA wire or coil is determined, the biasing element can be designed. In the case of a biasing compliant mechanism, the flexure hinges can be designed based on the desired stroke of the application. As fig. 3.4 details, the operating points must be estimated using the design of the compliant mechanism. The structure and design of the compliant mechanism can be used to determine the relationship between the strain recoverd by the SME and rotation of the flexural hinges, $\theta(x)$. This relationship can be used to determine the force-displacement curve of the resulting biasing element using the equation presented in eq. (3.1). Finally, the individual flexural hinges can be adjusted such that the desired stroke,x, is obtained and that the maximum pull force of the SMA wire or coil is not exceeded.

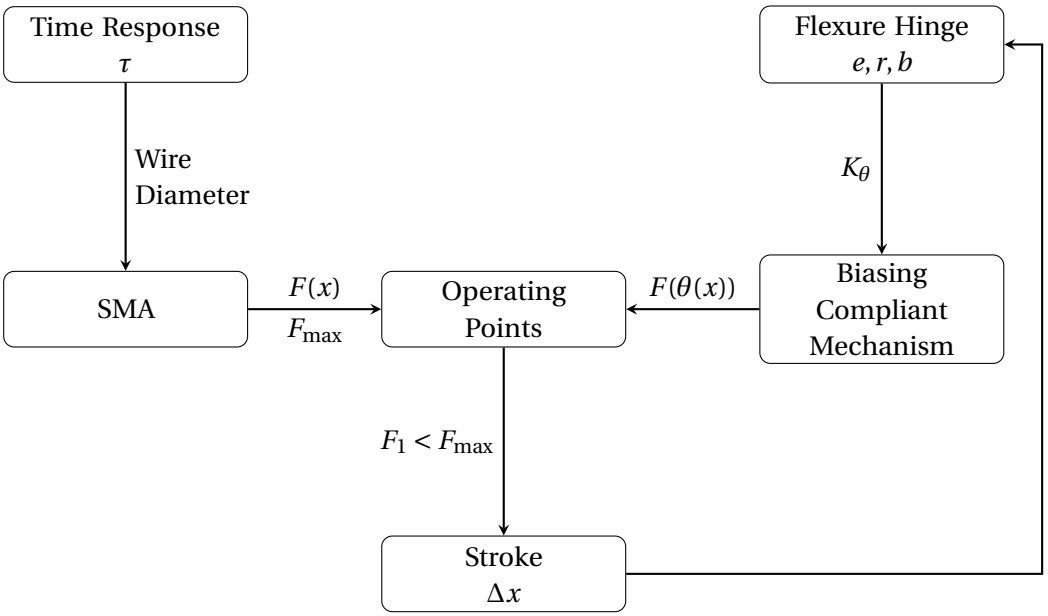

Figure 3.4: Design methodology for sizing biased-compliant mechanism SMA actuators.

Flexure-based hinges, however, exhibit a limited anuglar stroke. The maximum angle allowed before plastic deformation occurs has to be considered when designing such hinges. This admissible deformation, as described in the work by Henein (2005), can be calculated using :

$$\Delta\theta_{\text{adm}} \cong \frac{3\pi\sigma_{\text{adm}}\sqrt{r}}{4E\sqrt{e}} \tag{3.4}$$

By using the relationship between the input displacement and the hinge rotation, $\theta(x)$, the maximum admission stroke of the compliant mechanism, Δx_{adm}, can be computed. With this theoretical model complete, the entire mechanism can be sized such that the output stroke is maximised while avoiding failures during the deformation of the biasing compliant mechanism.

With $\mathbb{X}_{\text{eq}}$ being the set of possible equilibrium positions (see fig. 3.3) and $\mathbb{X}_{\text{el}}$ being the set of admissible positions for elastic deformation as defined below :

$$\mathbb{X}_{\text{eq}} = \{x \mid x_2 \leqslant x \leqslant x_1\} \tag{3.5}$$

$$\mathbb{X}_{\text{el}} = \left\{x \mid x_{\text{off}} - \frac{\Delta x_{\text{adm}}}{2} \leqslant x \leqslant x_{\text{off}} + \frac{\Delta x_{\text{adm}}}{2}\right\} \tag{3.6}$$

The set of feasible operating points for the biased-compliant mechanism SMA actuator, $\mathbb{X}_{\text{f}}$, is given by their intersection:

$$\mathbb{X}_{\text{f}} = \mathbb{X}_{\text{eq}} \cap \mathbb{X}_{\text{el}}. \tag{3.7}$$

Using this principle, if the mechanism is designed such that $\mathbb{X}_{eq} \subseteq \mathbb{X}_{el}$, then, the safety of the flexure hinges will not depend on precise control of the SMA which can be difficult to achieve. Furthermore, using these principle, various design trade-offs can be deduced, as shown in table 3.1

Table 3.1: The trade-offs observed during the sizing of the biasing compliant mechanism for the SMA actuator with a given SMA wire or coil. Here, S_{mech} and t_{mech} are the surface area and the thickness of the compliant mechanism, respectively.

Parameter	Effects	
$\frac{e}{r} \uparrow$	$\Delta\theta_{adm} \downarrow \Rightarrow \mathbb{X}_{el} \downarrow$	$K_\theta \uparrow \Rightarrow \begin{cases} \mathbb{X}_{eq} \uparrow \\ F_{grip} \downarrow \end{cases}$
$e \uparrow \mid \frac{e}{r}$ fixed	$S_{mech} \uparrow$	
$b \uparrow$	$t_{mech} \uparrow$	
$x_{off} \uparrow$	$\mathbb{X}_{eq} \uparrow$, $\mathbb{X}_{el}$ shifted away from $\mathbb{X}_{eq}$	

3.4.2 Integration of Compliant Mechanisms in Antagonistic SMA Actuators

The concept of augmenting traditional bias-spring SMA actuators with compliant mechanisms can be extended to Antagonistic SMA actuators. Traditionally, these actuators consist of a pair of active SMA elements where the SMAs are heated and cooled alternately. These actuators are relatively more complex due to the nonlinear nature of the SME. But, antagonistic SMA actuators have the advantage of an additional degree of freedom during activation. As the first SMA is heated, the antagonistic SMA is deformed and activated. Similarly, only upon heating the antagonistic SMA will the actuator be actuated in the opposite direction.

As with most SMA actuators fabricated using SMA wires or coils, the actuation of the actuator results in a linear motion. In application where complex motions are required, the antagonistic SMA actuator is paired with a kinematic stage that converts the linear movement to the required complex motion. Furthermore, they can be implemented into these antagonistic SMA actuators such that they present different behaviours based on the direction of actuation. As mentioned previously, flexure-based kinematic stages have the advantage of increased precision and reduced weight but presents with an inherent stiffness. Thus, this increased rigidity must be taken into account when sizing the SMA active elements.

In the traditional antagonistic SMA actuator, the first SMA, when heated and returns to its original length, deforms the antagonistic SMA. Thus, in this case, the heated SMA must overcome the rigidity of the cold SMA. The operating points of such a system can be deduced by taking the intersections between the hot and cold SMA curves as shown in chapter cite. In the case of a compliant mechanism, the system is connected to both SMAs at all times. Thus, the inherent stiffness of the compliant mechanism must be taken into account when actuated both SMAs. Therefore, the force-displacement curve of the compliant mechanism, $F_C(x)$, can be added to the curve of the antagonistic cold SMA, $F(x)$, to obtain the apparent

load observed by the heated SMA, as shown in fig. 3.5. The design methodology can thus be adjusted, as shown in fig. 3.6, such that when the SMA elements are sized and operating points are determined, no unintended behaviours occur. It is important to note that due to the complexity of the compliant mechanism curves, these unintended operating points can emerge causing shorter strokes.

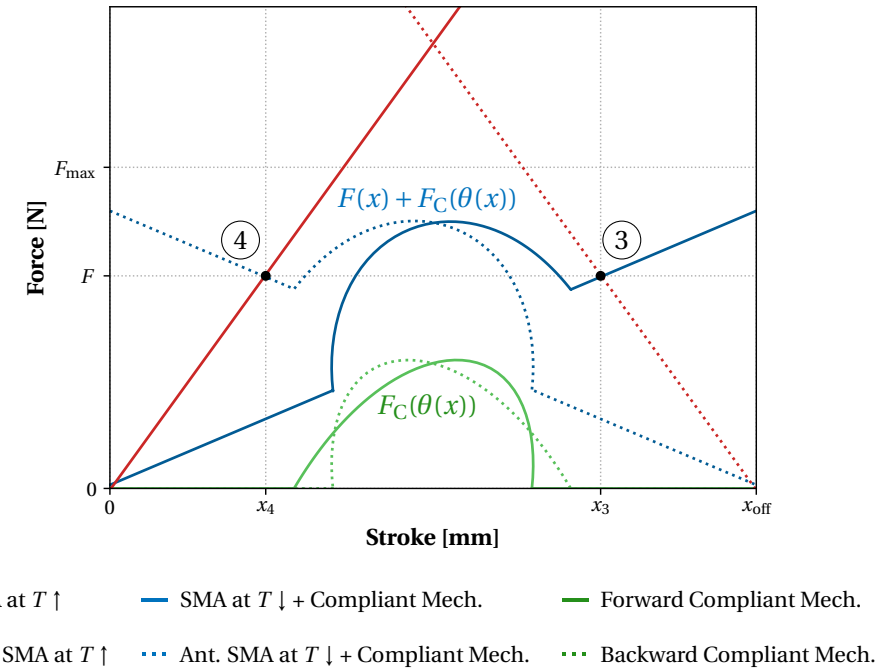

Figure 3.5: The adapted sizing methodology of an antagonistic SMA actuator paired with compliant mechanism using the simplified SMA curves.

In summary, as illustrated in fig. 3.6, the design methodology consists of deriving the force-displacement curves of the SMA elements and the relationship between the input displacement, x, and the hinge rotation, $\theta(x)$. Once these relationships are deduced, the force-displacement relationship of the compliant mechanism, $F_C(\theta(x))$ can be added to the force-displacement curve of the cold antagonistic SMA element. An important parameter to note is the prestretched length, x_{off} of the SMAs. As the SMA is prestretched, when heated, the SMA can exert higher levels of force but could result in forces that exceed F_{max}. Using the two curves, the operating points can be estimated and verified such that the resulting stroke, Δx, fits within the requirements of the application. Furthermore, the geometric parameters of the hinge design of the compliant mechanism can be adjusted such that there are no unintended operating points and that the maximum pull force of the SMA is not exceeded.

Recently, there has been considerable work in developing bistable or multistable actuators. These actuators are able to main a stable position without required any holding energy. This property could be highly beneficial in applications such as grippers. Here, the gripper can stay in the open or closed position without requiring any additional energy. These bistable systems

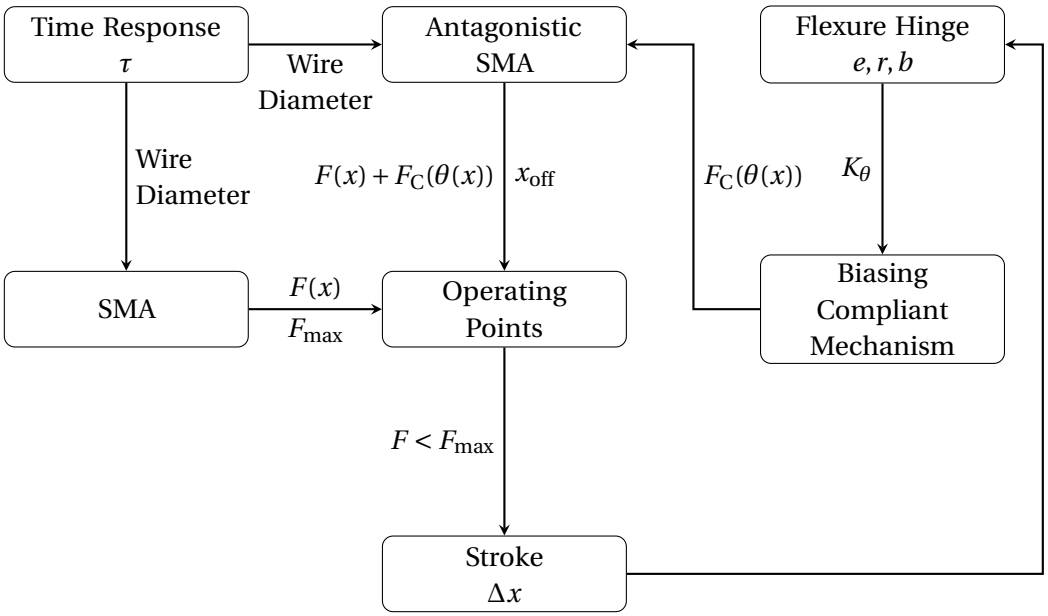

Figure 3.6: Design methodology for sizing antagonistic SMA actuators paired with compliant mechanism.

can be created using flexure-based structures, as shown in the work by Jin Qiu et al. (2004). A axially compressed cantilever beam exhibits bistability and has been implemented in various smart material actuators. In the work by Chouinard and Plante (2012), a dielectric elastomer actuator is paired with a buckled beam to create a compact bistable actuator. Furthermore, in the work by Zhang et al. (2020), a bistable drone-ready gripper is fabricated and is actuator using an electric motor. This principle can be implemented and actuated using SMAs, as shown in the work by Welsch et al. (2018). However, the sizing of such a system are missing due to the complex nature of the bistable mechanism and the nonlinear nature of the SMA. Using the proposed, methodology, as shown in fig. 3.6, the SMA can be sized to present with higher time responses while still able to trigger the bistable positions of the actuator. The accurate sizing of such a bistable SMA actuator is validated later in section 6.3.

3.5 Summary and Conclusion

In this chapter, the traditional sizing methodology has been adapted to fit the case where biasing springs are replaced with passive biasing compliant mechanism. This approach stems from the concept where the traditional SMA actuators consisting of an active element, a biasing element and a kinematic stage is transformed into a more integrated solution where the biasing element and the kinematic stage are combined.

Using pseudo-rigid body models described in the work by Henein (2005), the analytical models of the compliant mechanisms are used to estimate the stroke and behaviour of the novel SMA actuator. Using the simplified SMA curves, these alloys can be sized such that the time

response of the SMA actuator is minimized.

Furthermore, this novel approach to designing SMA actuators paired with compliant mechanisms has been adapted for antagonistic SMA actuators. By altering the design methodology, the often used antagonistic SMA actuators can be sized such that when paired with compliant mechanisms, the actuator does not present any unintended behaviours and reduces the time response.

Most SMA actuators that make use of kinematic stages to convert the linear motion of the actuator into more complex behaviours, also integrate a passive spring in the design. By applying the presented design approach, SMA actuators can be designed such that compliant mechanisms can be used as biasing elements. This methodology will be further validated using case studies in chapter 6.

4 Designing Actuators Powered by Compliant SMA Elements

4.1 Introduction

Smart materials, due to their integrated nature of reacting mechanically to a certain type of stimulus, have become an integral part of designing complex actuators. These materials have become an integral part of designing integrated and compact actuators. As presented in chapter 3, integrating the traditional building blocks of the tradition smart actuator can results in more compact designs. The behaviours of smart materials, however, range from simple linear behaviours to highly complex multi-physical behaviours. Thus, designing smart actuators with complex geometries are only feasible with certain types of smart materials.

In the case of shape memory alloys, the shape memory effect is a complex non-linear behaviour that is reliant on multiple kind of physics. This results in active elements present in SMA actuators to often be in the shape of wire, coil or thin sheets. These 1-dimensional structures are the most common type of implementation in SMA actuators due to the fact that their behaviours when heated or cooled are more easily predicted. As stated, in practice, when complex motions are required, the actuator is composed of complex kinematic stages and a simple SMA wire or coil as shown in the work by cite.

When taking inspiration from other more established smart materials, complex designs that still exhibit the smart behaviours of the material are often generated using algorithm as shown in the work by cite. Topology Optimization (TO) has been essential in designing such complex design that can take simple inputs and transform them into more complex and useful outputs. These compliant mechanisms fabricated from smart materials are compact and lightweight. However, combining this design methodology with SMAs can be quite difficult and computationally expensive to implement due to the highly non-linear nature of the Shape Memory Effect (SME).

In this chapter, a robust design methodology to design compliant SMA structures for powering integrated smart actuator is presented. Furthermore, a qualitative factor is described that can be used to compare various generated SMA topologies. Using Finite Element Modelling

(FEM), the various topologies are simulated and shown to exhibit the shape memory effect.

4.2 Designing Integrated Active Elements

When designing smart actuators that display complex output motions, they generally consist of 1D SMA structures such as wires coupled with complex kinematic stages that transform the simple linear motion into complex ones, as shown in the work by citeand cite. By extrapolating the methodology presented in chapter 3, it is conceivable to imagine a scenario where the active SMA elements and the kinematic stages are combined, as shown in fig. 4.1. Here, compliant structures fabricated from a monolithic block of SMA can be used to create compact actuator that no longer require a kinematic stage consisting of multiple pieces.

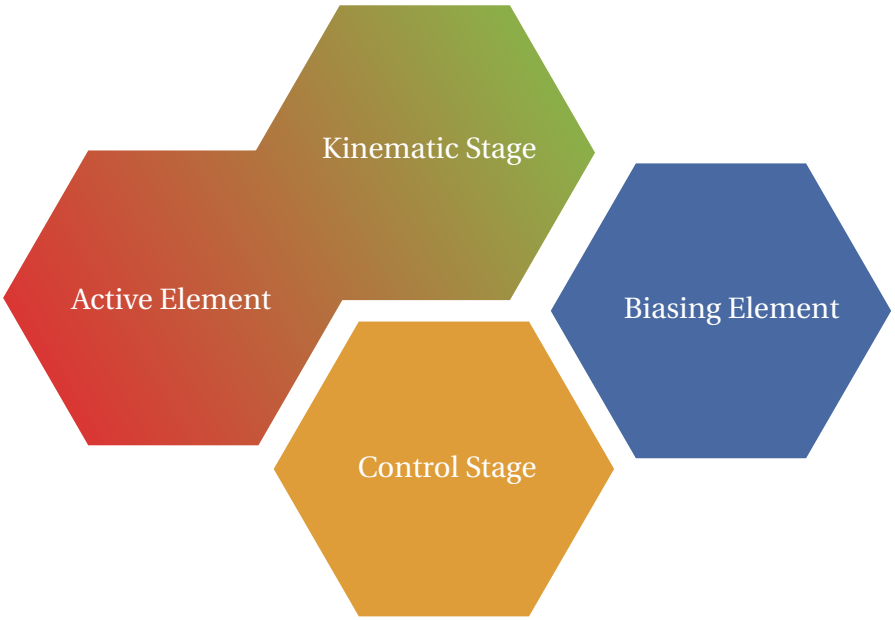

Figure 4.1: Diagram of the adapted building blocks of the SMA actuator based on integrating the active element and the kinematic stage.

The challenges posed by this approach consist of the complex nature of the shape memory effect. The behaviour, consisting of highly non-linear behaviour and comprised of multi-physical variables, makes it hard to predict when the complex geometries are heated or cooled. Furthermore, implementing generative algorithms that design these complex geometries, as implemented with other simpler smart materials, is difficult due to the high computational costs required to simulate the shape memory effect.

4.3 Designing with Topology Optimization

Due to the high computational costs of simulating the shape memory effect, it is quite difficult to generate complex novel geometries even with poor mesh resolution. The basic principle of the proposed approach is to generate novel designs made of SMAs with computer-aided methods such as topology optimisation method (TOM). Here, the crux of the approach consists of abstracting the temperature-dependent effects but appropriately formulate the design problem so as to indirectly take into account the requirements of the shape memory effect.

When purely optimising for strain and assuming a standard elastic material, compliant mechanisms can be designed without considering the nonlinear nature of the material. Here, as mentioned previously, the requirements of the shape memory effect consists of a certain level of deformation during lower temperatures. Thus, the optimisation, when designing the compliant structure that when exposed to a biasing element, prioritises the strain across the entire structure. As long as the material undergoes sufficient deformation, above a critical strain threshold, will exhibit the shape memory effect when heated to higher temperatures. The analysis is executed assuming small and purely elastic deformation to reply on linear finite element analysis so as to significantly reduce the computational time.

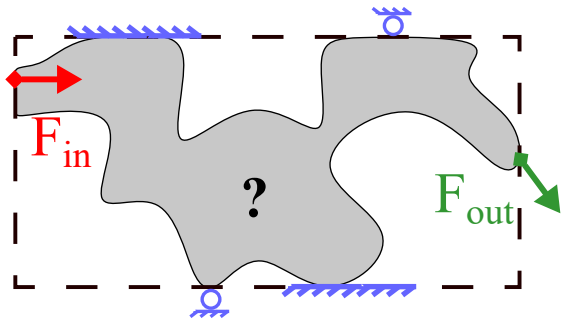

Figure 4.2: Basic design problem for compliant mechanisms.

4.3.1 Density-Based Topology Optimization

The basic concept being topology optimisation consists of investigating the distribution of material inside a discretised design space while trying to improve a certain specified objective function. The design variables applied in this density-based approach optimisation are artificial densities ρ that describe the proportion of the material, $0 < \rho_{\min} \leq \rho \leq 1$, an individual domain space is filled with. The lower and upper bounds of density range are considered as *full* materials representing fully empty or fully filled elements, respectively. While the densities within the range are defined as *intermediate* materials. Here, this artificial density variable are made continuous to use a gradient-based solver which has the advantage of lower computational time compared to non-gradient based approaches, as shown in the work by Sigmund (2011). In order to avoid mesh-dependent solutions and checker-board patters, the optimisation is regulated. This is achieved with a density filter that limits the length scale, $r_{\min}$,

to a minimum inside the structure, as shown in the work by Bendsoe and Sigmund (2013).

Each iteration of the optimisation consists of the following steps. First, the filtered design variables are mapped to a material property using the Material Interpolation Scheme (MIS). This converts the artificial densities into a usable Young's Modulus. Next, the well-known Solid Isotropic Material Penalisation (SIMP), as shown in eq. (4.1) from the work by Bendsoe and Sigmund (2013), is implemented. This scheme penalises intermediate materials so as to prevent obtaining a geometry that cannot be manufactured. This is done using a penalty facor n which continuously increases throughout the optimisation.

$$\mathrm{E}_e = \mathrm{MIS}(\rho_e) = (\overline{\mathrm{E}} - \underline{\mathrm{E}})\rho_e^n + \underline{\mathrm{E}}, \tag{4.1}$$

with $\underline{\mathrm{E}}$, $\overline{\mathrm{E}}$ the lower and upper bound of $\vec{\mathrm{E}} = [\mathrm{E}, \cdots, \mathrm{E}_{\mathrm{NE}}]^{\mathrm{T}}$ respectively corresponding to the Young's modulus of an "empty" element and a completely filled one. NE is the number of elements inside the domain. When the material properties of each element are known, the *Stiffness matrix* K of the corresponding structure is constructed. Next, Finite Element Analysis (FEA) is performed to estimate the displacement U of each node under imposed external loads F so as to solve the linear elasticity equation: KU = F. The chosen objective function with its associated sensitivity (gradient of the objective function with respect to the design variable) is evaluated using these, aforementioned, displacements. For the following iteration, the sensitivities can, then, be used by the solver to update the design variables. In this case, the Optimality Criteria (OC) scheme from the work by Bendsoe and Sigmund (2013) is used as the solver.

One of the main advantages to this approach to designing compliant SMA elements is the fact that various Open-Source academic codes are available for implementing this structural topology optimisation as shown in the work by Zhu et al. (2020) and Talischi et al. (2012). Due to ignoring the thermal dependencies of the shape memory effect, the resulting FEA used is similar to that of traditional compliant mechanisms and can thus be easily extended to such generative algorithms by simply changing the objective functions and associated sensitivity.

4.3.2 Topology Optimization of Compliant Mechanisms

The basic principle behind designing a compliant mechanism, as illustrated in fig. 4.2, can be formulated as : "Under an external input force and certain boundary conditions, what is the distribution of material defining the compliant mechanism that transforms the input load to a specific output one?"

At the input and output points, artificial springs are added to simulate the input work and resistance to the output displacement of the workpiece, respectively, as shown in the work by Alonso et al. (2014). In the final geometry, these springs are removed and are only present during the design process. Regarding the objective function that governs the final design of the compliant mechanism, a formulation that can be extended to Multi-Input Multi-Outputs

(MIMO), is implemented based on various strain energies as shown in the work by Alonso et al. (2014).

An objective function based upon the mutual strain energy between the input and output is chosen. This permits to distribute the strain throughout the structure and avoid to have only *de facto* (single point) hinges responsible for the compliant behaviour. Ideally, the maximum volume of the structure should be deformed to harvest as maximum work, when the alloy is heated and experiences the shape memory effect. Here, the objective function is built using three different types of strain energies. First, there is the input strain energy S_{in}, that is present when only an input load F_{in} is applied and result in some nodal displacements U_{in}. Similarly, the output strain energy S_{out}, is present when only a dummy unit load F_{out} is applied at the output port resulting in nodal displacements U_{out}. Finally, the Mutual Potential Energy (MPE) or mutual strain energy S_{mut} can be built with the two previous nodal displacements. The objective function is chosen as a ratio of these three energies due to its non-dimensional aspect and due to the fact that the desired input and output displacements are indirectly accounted for. Here, since the problem is formulated as a minimisation, a minus signed is placed before the chosen ratio to maximise the MPE as follows :

$$\gamma = -\frac{S_{mut}}{S_{in} + S_{out}} = -\frac{{U_{out}}^T K U_{int}}{\frac{1}{2}{U_{out}}^T K U_{out} + \frac{1}{2}{U_{in}}^T K U_{in}}. \tag{4.2}$$

Lastly, two separate FEAs are performed to evaluate the chosen objective: $KU_{in} = F_{in}$ and $KU_{out} = F_{out}$.

The current objective governing the design of the generated compliant mechanisms made of *conventional* linear material, can be extended to generating design for mechanisms made from SMAs. This is due to the fact that, as previously mentioned, the algorithm tends to distribute the strain throughout the structure which will indirectly allow a large portion of the material to be activated if made from SMA. The optimisation problem, as formulated in eq. (4.3), consists of the minimisation of the objective function γ subject to the limitation of the infill Vol^* of the design domain's volume, with V_e the volume of element e.

$$\begin{aligned} \min_{\vec{\rho}} : \quad & \gamma(\vec{U_{in}}, \vec{U_{out}}, \vec{E}) \\ \text{s.t. :} \quad & KU_{in} = F_{in} \\ & KU_{out} = F_{out} \\ & Vol < Vol^*, \text{ with } Vol = (\sum_{e=1}^{NE} \rho_e \cdot V_e)/(\sum_{e=1}^{NE} V_e) \\ & \vec{E} = MIS(\vec{\rho}) \quad 0 < \rho_{min} \leqslant \rho \leqslant 1. \end{aligned} \tag{4.3}$$

In fig. 4.3, the basic design problem is displayed using the common force inverter scenario.

Due to the symmetry of the problem, the domain space can be restricted to half the surface while adding rolling supports at the symmetry axis. In fig. 4.4, the evolution of the optimisation can be observed. Here the domain space is uniformly initialised with intermediate materials such that the volume limitation is satisfied so as to have the design converge to a solution that is only composed of full materials.

4.4 Benchmark problems

Before designing complex multi-output compliant SMA elements, the shape memory effect of the generated geometries must be validated. In this regard, a common practice is to use some traditional benchmark problems. The problems, while being simple problems, can be used to validate the generated designs using a commercially available Finite Element Modelling (FEM) software such as ANSYS®. Using an FEM, the shape memory effect of the generated topologies can be simulated, verifying the efficiency of the algorithm for designing compliant SMA mechanisms.

The proposed design method is applied to three benchmark problems : an inverter, a crimper, and a gripper. They are all fixed at their bottom and top left corners (which corresponds to ideal pivots) but each have their own input and output forces. The design problems and the resulting geometries are shown in fig. 4.3, fig. 4.5, and fig. 4.6. This half domain space has been discretised into 10^4 elements and the design variables are initialised uniformly with a volume fraction constraint of 30%. The stiffness of each artificial spring is equal to 0.1 and the input forces are equal to 1. When run on a Windows workstation with an Intel i7 3.6 GHz, 8-core processor and 32 GB of memory, the complete process takes less than 1 minute to converge to solution. It is important to note that the computational time would have been significantly higher if a non-linear and multi-physic analysis was executed. Due to the short computational time, this design method can be extended to 3-Dimensional problems.

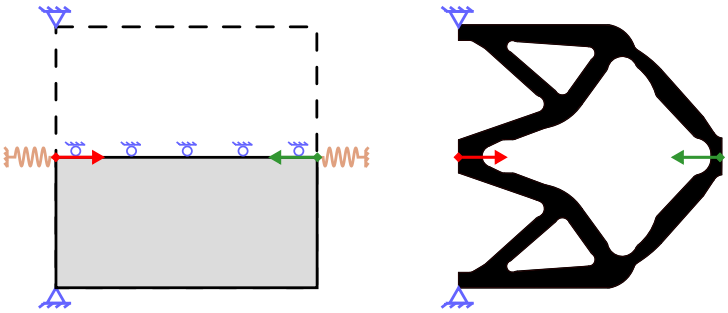

Figure 4.3: Inverter: Design problem (left), Interpolated final topology (right). Input force is shown in red while the output force is shown green.

Here, in the hopes of validating the shape memory effect, a four time-step simulation is constructed. The four different simulated steps can be seen in fig. 4.7. Here, the figures represent the results of the FEM simulation for each benchmark problem. The simulation

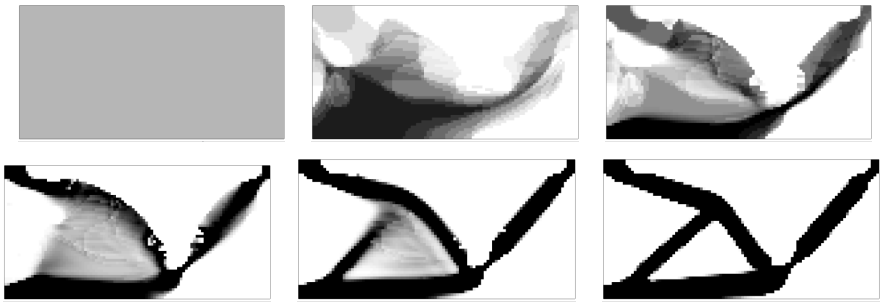

Figure 4.4: Evolution of the inverter design throughout the optimization. The grayscale represent the value of the filtered artificial density.

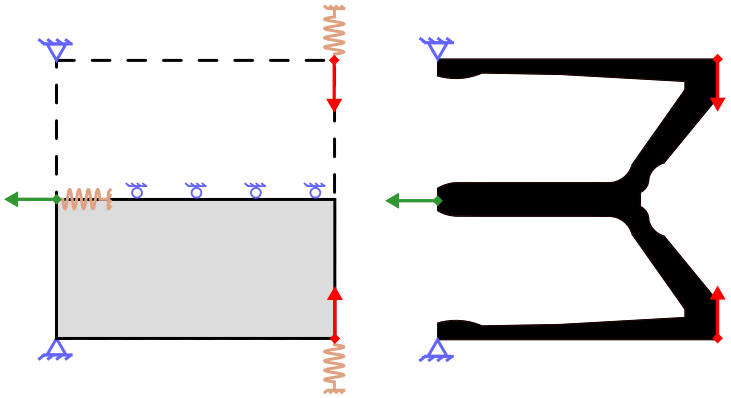

Figure 4.5: Crimper: Design problem (left), Interpolated final topology (right). Input force is shown in red while the output force is shown green.

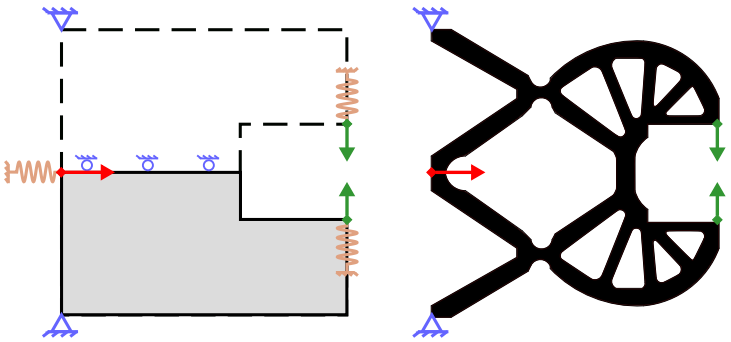

Figure 4.6: Gripper: Design problem (left), Interpolated final topology (right). Input force is shown in red while the output force is shown green.

consists of first applying an input displacement which generates a displacement at the output, $\varepsilon_{\text{loaded}}$. If the entire structure is sufficiently strained to undergo the detwinning process, as explained in chapter cite, the structure will keep its deformed shape when the input displacement constraint is released. However, as some areas of the compliant structure does not undergo detwinning, a portion of the strain will be lost when the constraint is released. Thus, the observed strain at the output will decrease to $\varepsilon_{\text{free}}$. During the third time step, the

structure is heated to activate the shape memory effect and force the structure to revert back to its original shape where all the strain is recovered. Finally, the structure is allowed to cool down and return the material back to its martensitic phase.

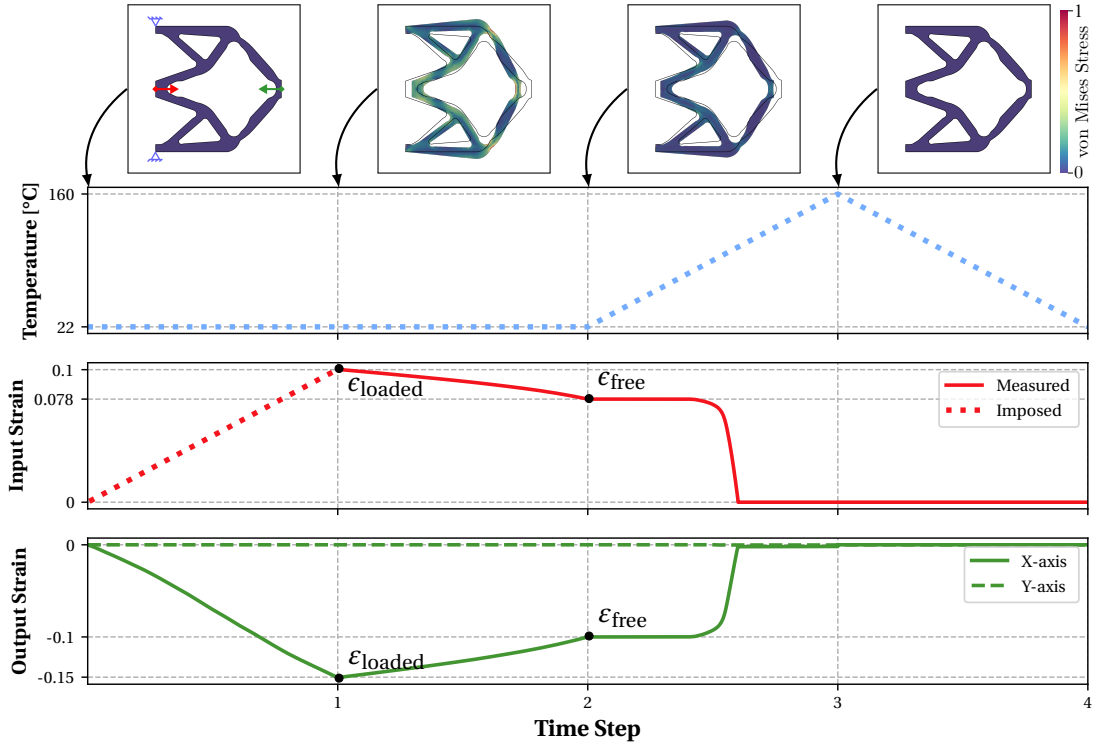

Figure 4.7: Results of the shape memory effect simulation of the Inverter design. Here, the displacements are calculated relatively to the design domain size L. The displacements observed between time steps 1 and 2 show a strain retention of $\alpha_\epsilon = 77.6\%$ confirming the presence of the shape memory effect.

4.4.1 A Qualitative Measure of the SME

Since the topologies generated by the algorithm are widely different consisting of varying inputs, outputs and geometries, a measure by which the results can be compared is required. The final goal, being to integrate these compliant mechanisms as the active element in a biased-spring SMA actuator, the measure should represent the degree to which work has been stored by the biasing element. This measurement factor could be formulated as a measure of the relative quantity of material activate (or detwinned) by the biasing element. This implies that the larger the value of the factor is, the more optimal the biased-actuator will perform.

The amount of detwinned material in the geometry can be roughly estimated using the principle that the deformed material behaves plastically. In other words, it is the volume of the material that is able to retain its shape after the load has been released. This factor, as described in eq. (4.4), is expressed as the strain retention factor and is defined as the amount

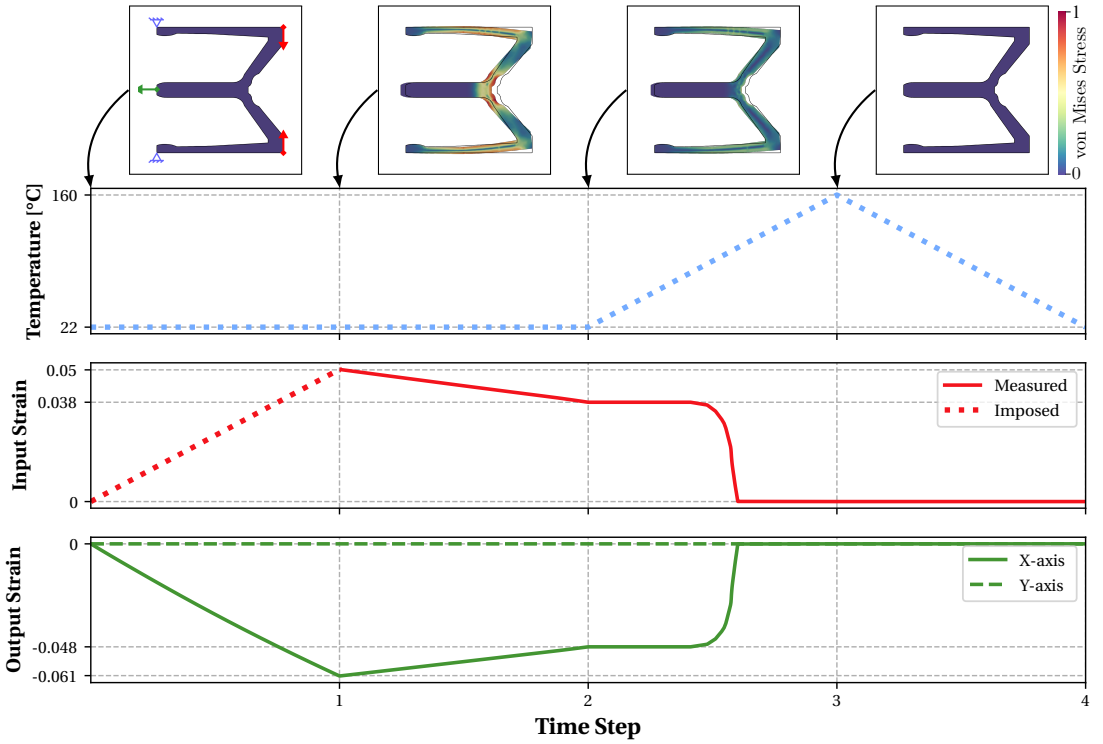

Figure 4.8: Results of the shape memory effect simulation of the Crimper design showing a strain retention of $\alpha_\epsilon = 75.2\%$.

of strain observed in the topology after the deformation load is released. This factor will vary between 0 implying non of the material has been activated and the topology retains completely back to its original shape when the load is released and 1 for a perfectly detwinned material where the entirety of the strain is retained and can only be reverted back to its original shape when heated. This strain retention factor can be calculated using :

$$\alpha_\epsilon = 1 - \frac{\epsilon_{\text{loaded}} - \epsilon_{\text{free}}}{\epsilon_{\text{loaded}}}, \tag{4.4}$$

with ϵ_{loaded} and ϵ_{free} representing the domain space normalised input displacement at time step 1 and 2 respectively. It is important to note that this factor can never be equal to 1 as there is some natural elastic spring back of the material even when fully detwinned and thus, is only a qualitative measure of the shape memory capabilities of the topology. It is still an effective way to compare the different topologies presented using the benchmark problems. The FEM results of the strain retention of each benchmark problem can be seen in table 4.1. This principle can be further extended to more complex designs where goal is to create compliant SMA structures that can have multiple outputs using just a single input biasing element which will be presented in future sections.

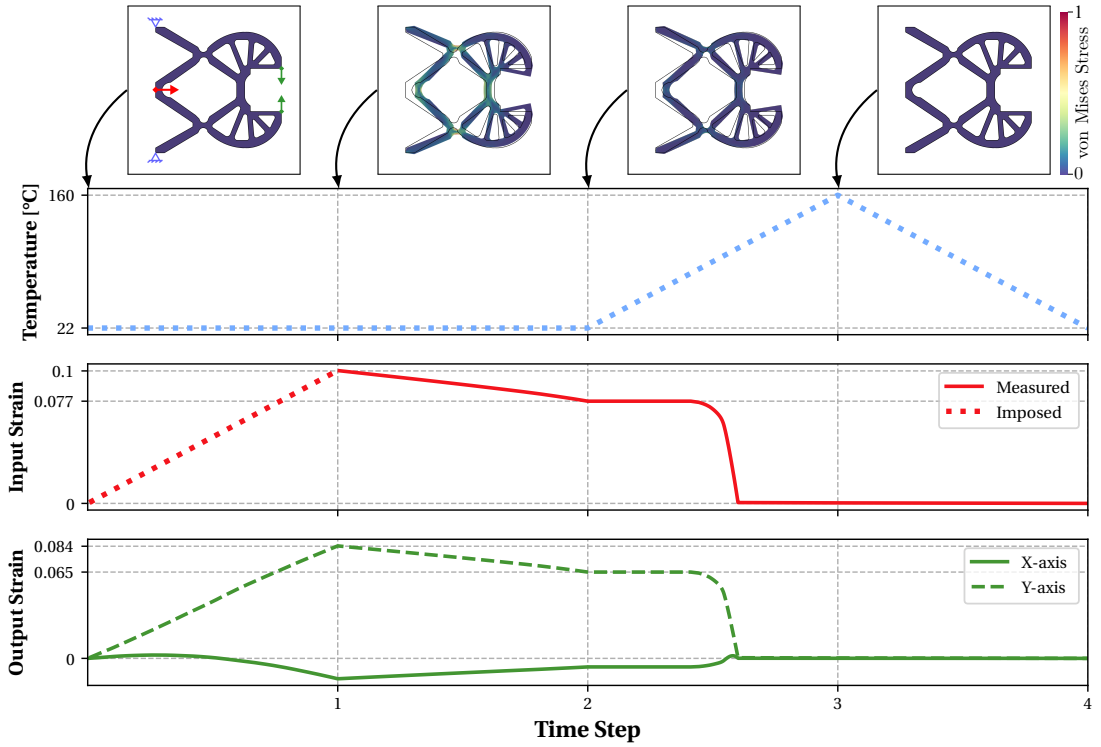

Figure 4.9: Results of the shape memory effect simulation of the Inverter design showing a strain retention of $\alpha_\epsilon = 77.6\%$.

Table 4.1: The simulation results of the strain retention factor for each of the benchmark problems: $\mathscr{I}$ Inverter; $\mathscr{C}$ Crimper; $\mathscr{G}$ Gripper

	$\varepsilon^x_{\text{loaded}}$	$\varepsilon^y_{\text{loaded}}$	$\varepsilon^x_{\text{free}}$	$\varepsilon^y_{\text{free}}$	α^x_ϵ	α^x_ϵ
$\mathscr{I}$	0.149	-	0.103	-	**77.6%**	-
$\mathscr{C}$	−0.061	-	−0.048	-	-	**75.2%**
$\mathscr{G}$	0.015	−0.085	0	−0.065	**77.6%**	-

4.4.2 Experimental Validation of the Methodology

In the previous section, three benchmark problems were used to validate the presence of the shape memory effect of topologically optimised compliant structures made from SMAs. Furthermore, a qualitative measure was formulated so as to compare and assess the degree to which these compliant structures would be ideal in creating biased-spring SMA actuators. However, to truly verify the presence of the shape memory effect, an experimental prototype can be fabricated.

For an accurate comparison between the FEM results and the experimental data, a prototype of a benchmark problem is conceived. For the sake of simplicity, the inverter problem is chosen

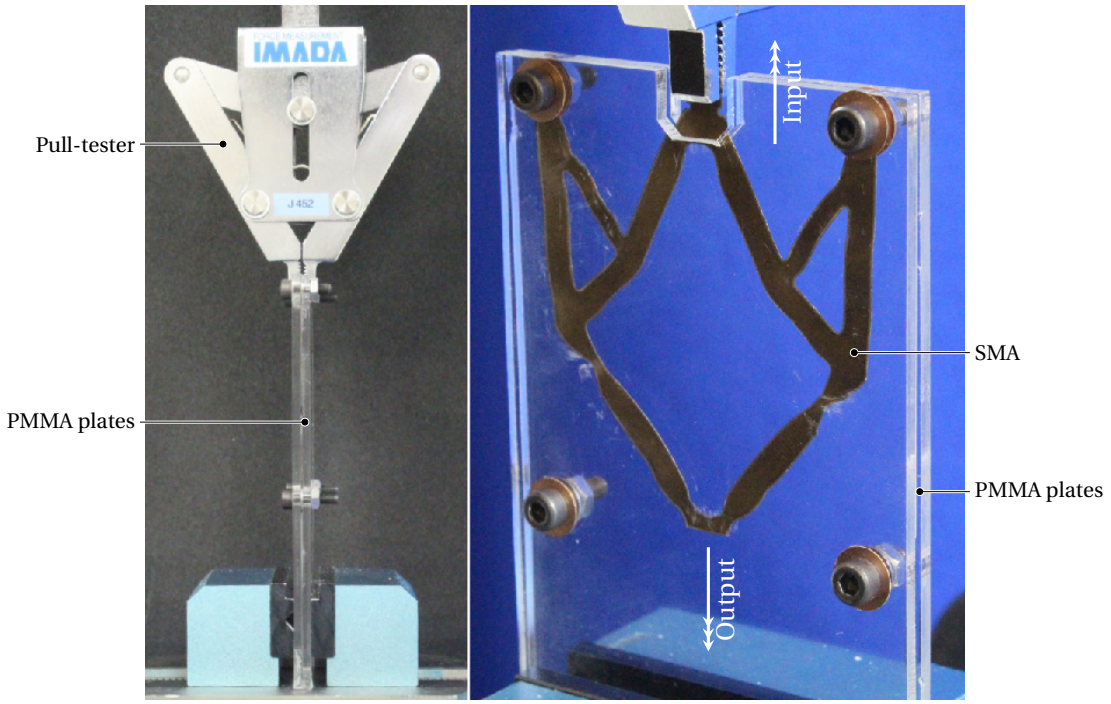

Figure 4.10: The experimental setup of the inverter prototype. The prototype is cut from a thin SMA sheet and is sandwiched between PMMA sheets to prevent buckling. The input load is applied using the pull-tester while measuring the input displacement and force. The output displacement is recorded using a microscopic camera.

due to the fact that there is only one input and output. When designing the inverter, ideal pivots are used. However when creating the experimental prototype, these ideal pivots are changed to a more realistic solution involving mounting holes. Based on these new boundary conditions, the inverter problem is redesigned using the proposed topology optimisation algorithm.

When fabricating the prototype, the cost of machining a monolithic block of NiTiNOL was deemed unfeasible. With the advent of additive manufacturing of NiTiNOL as portrayed in the work by cite, the creation of such compliant mechanisms has become cheaper and more feasible. However, in this case, as the topology generative is 2-Dimensional, the inverter prototype was fabricated by laser cutting thin sheets of NiTiNOL (55.8 wt. % Ni). This laser cut inverter structure was then sandwiched between two PMMA sheets to prevent any unwanted buckling in the third dimension, as shown in fig. 4.10. This ensures that the deformations observed within the structure resembles the simulation.

The advantages of such a implementation, to test the validity of the design methodology, include the reduced cost of the prototype and more importantly, ensuring that the stress and strain distribution within the 2D structure is identical to the simulated 3D structure. This implies that the output displacement of the inverter prototype will closely resemble that of the simulated structure. The main disadvantage of this implement comes from the

fact that the PMMA sheets cause lots of friction with the compliant structure. This implies that force requirements at the input will be higher than expect. As we sandwich the PMMA sheets more tightly around the compliant structure, the output displacements will be more accurate while increase the friction and force requirements to create the aforementioned output displacement. Thus, a trade-off is present but the strain retention factor, as described in eq. (4.4), is only dependent on the the displacement and not the force requirements. Thus, the prototype was fabricated to maximise the input and output fidelity rather than the force requirement. Here, a pull-tester is used to measure the displacement of the input and the force requirements.

The goal of this section is to experimentally validate the proposed design methodology. The prototype of the compliant SMA benchmark problem was realised and must be compared to the results of the simulation. As described before, the strain retention factor was developed to compare the various generated topologies and to have a qualitative analysis of the structure to be used as a bias-spring SMA actuator. Thus, this factor can also be used to compare the experimental prototype of the modified inverter mechanism and its corresponding FEM simulation.

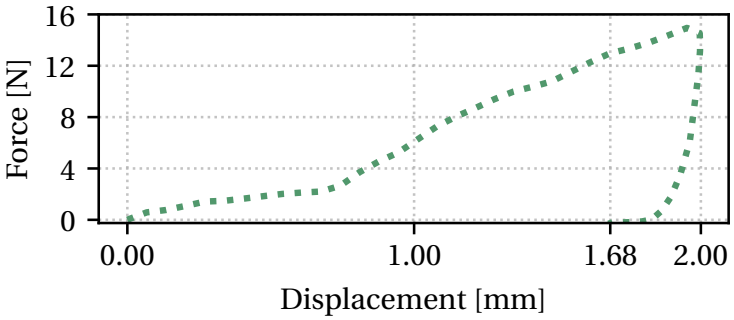

Figure 4.11: The experimental results of the inverter prototype are obtained using a pull-tester and a strain retention of 84.3% is observed.

In fig. 4.11, the pull-tester results can be seen. The strain retention is measured by applying an initial strain to the input of the prototype using the pull-tester. By then reversing the direction of the pull-tester and measuring the reaction force, the point at which the reaction force descends below 0 N will define the strain that is retained by the structure after the initial load is released. We assume that as the pull-tester observes a value below -0.2 N, the structure has overcome the internal friction with the PMMA sheets and is now bending the input of the prototype rather than returning to its original shape. Based on the values observed using the pull-tester, a strain retention of 84.2% is measured as shown in table 4.2. When comparing to the results of the simulation of the same modified inverter topology of 78.9%, the shape memory effect capabilities of topologies generated by this design approach is validated. The difference in the strain retention between the experimental and FEM results can be accounted by the friction present in the physical implementation.

Table 4.2: Comparison between the FEM and experimental results of the modified inverter benchmark problem.

	x_{loaded} [mm]	x_{free} [mm]	α_ϵ [%]
FEM	2.0	1.58	78.9
Expt.	2.0	1.68	84.3

4.5 Proposed Induction Heating Strategy

Due to the complex geometries of the generated topologies, simply passing a current through the structure by attaching electrode to the ends is no longer possible. In the case of inverter prototype, electrodes must be attached at multiple points so as to allow current to flow through all the areas of the geometry.

Various works have been established where surface mounted coils have been installed to function as a heating coil that raise the temperature of the SMA structures for localised heating, as shown in the work by cite. This can be quite cumbersome due to possible risks of delamination while the SMA contracts and dilates during actuation. Another option would be to use hot air as a medium to increase the temperature of the SMA structure, perhaps with tools such as hot air guns. These external heating structure drastically reduce the work density of the resulting actuator and are thus, rarely used in small and compact applications.

Due to the complex geometry of the inverter prototype, the current paths for Joule's heating are no longer unique, nor trivial anymore. Here, in this case, multiple electrodes with multiple external wires are required to heat the structure. Thus, here, the proposed heating solution consists of a contactless, wireless strategy where a current is induced within the SMA structures using external induction coils.

4.5.1 Magnetic Induction Heating

The basic working principle of the proposed heating methodology and its application in the inverter mechanism can be seen in cite. By passing an alternating current at a high frequency is passed through the primary coil and generates a magnetic field. When any electric conductor, the SMA structure in this case, is placed inside the generated magnetic field, a secondary electric current, I_{induced}, is induced inside the structure. This induced current will generate Joule's losses, P_{Joules}, heating the SMA :

$$P_{\text{Joules}} = R_{\text{SMA}} \cdot I^2_{\text{induced}} = \frac{V^2_{\text{emf}}}{R_{\text{SMA}}}. \tag{4.5}$$

The magnitude of the current is based on the electromotive force, V_{emf}, generated by the primary coil, and the effective resistance, R_{SMA}, of the path taken by the induced current. The

coupling between the primary coil and the SMA piece, as described in eq. (4.6), dictates the electromotive force.

$$V_{\text{emf}}^2 = \left(-\frac{d\Psi}{dt}\right)^2 = \left(-2\pi f L \cdot I_{\text{prim}}\right)^2 \tag{4.6}$$

where Ψ is the total flux linkage between the primary and SMA side, f is the working frequency, I_{prim} is the *RMS* value of the primary current and L is the mutual inductance between the primary coil and the SMA structure. As a voltage source is used to power the system, the input current is maximised and the resistance of the primary coil is minimised. This is further increased by creating a resonating circuit where a capacitor is connected to the primary coil.

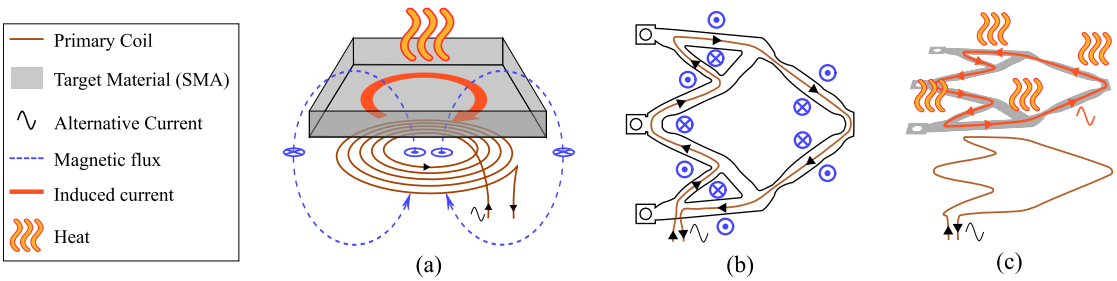

Figure 4.12: Induction heating - (a) General principle, (b) 2D view of the coil designed for the deformed inverter, with the direction of the generated magnetic flux normal to the plane, (c) 3D view of the induction system for the inverter problem.

When designing the heating solution for maximum induced current, as shown in eq. (4.6), a large working frequency is desired. However, when working with alternating currents at high frequencies, undesirable effects such as skin and proximity effects, arise which increase the resistance of the primary coil. Furthermore, the parasitic capacitance of the impedance of the coil will take over above a certain critical frequency, cancelling the inductive effect. By limiting the working frequency, a favourable balance between the losses at the primary coil and the induced current at the resonant value can be maintained. The mutual inductance between the primary coil and the SMA structure can be maximised for a large area of influence and a large number of turns. However, the area of influence cannot be increased as it is constrained by the shape of the generated SMA topology while the number of turns is limited by the associated increase in resistance which in turn reduces the magnitude of the input current. Thus, based on the application, the sizing of the primary coil comes with various trade-offs.

4.5.2 Fabrication and Results of Primary Coil

Due to the complex shape of the generated SMA topologies, the shape of the primary coil must be designed so as to induce a current path across the deformed regions of the compliant mechanism. Currently, the fabrication of the primary coil is performed by hand using nails and a wooden plate. The nails are used to create the shape based on the desired current path and a wire is wound around the nails to fabricate the coil. Once constructed, varnish is used to maintain the shape of the primary coil when the nails are removed. As shown in fig. 4.13, two types of primary coils are constructed using 25 turns a standard monolithic wire with a

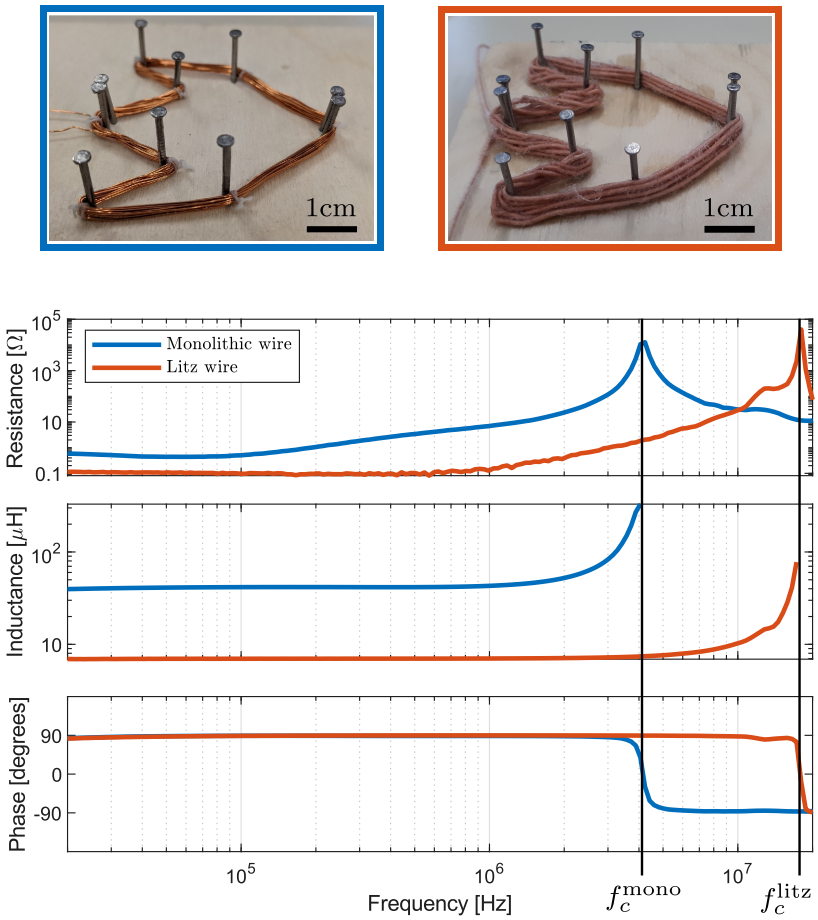

Figure 4.13: Comparison of primary coil with different types of wire. As the impedance becomes mainly capacitive over its critical frequency, the inductance's values after $f_c^{\text{mono}} =$ 17MHz and $f_c^{\text{litz}} = 41$MHz are removed for the monolithic and Litz wire respectively.

copper diameter of 0.30mm, and another composed of 15 turns of a Litz wire composed of 300 strands with a diameter of 0.040mm each. As shown in fig. 4.13, the resistance of tbe wire increases significantly with the frequency due to the skin and proximity effects. This implies that a thinner effective cross-section is preferred, as in the case of the Litz wire.

As mentioned previously, the working frequency plays an important role in this proposed heating system. A trade-off is present where a higher value increases the heating but also increase the parasitic capacitance of the coil, limiting the impedance above a critical frequency, $f_c^{\text{mono}} = 17$MHz and $f_c^{\text{litz}} = 41$MHz for the coil made of monolithic and Litz wire, respectively. As shown, despite the lower inductance of the Litz coil, better heating performance is achieved due to the working frequency and higher primary current when compared to the monolithic wire.

Here a working frequency of around 4 Mhz has been chosen so as to ensure that it sits safely above the critical frequency. At this frequency, the inductance of the coil is $L = 7.4$ μH and its

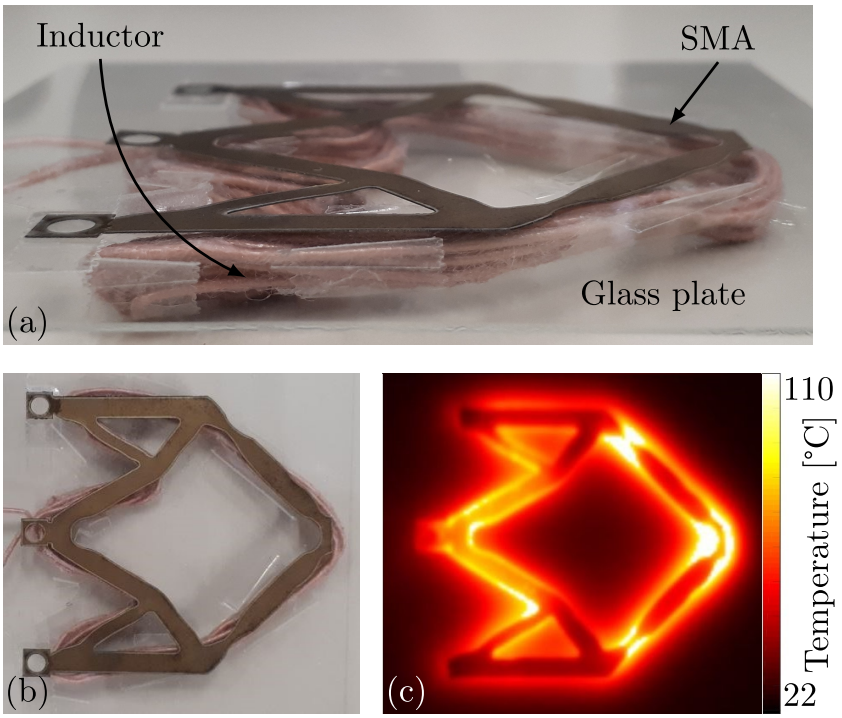

Figure 4.14: Implementation of induction heating system. When activated, it resulted in the heating of the SMA structure, reverted the deformed structure back to its original shape.

resistance $R = 0.4\ \Omega$. A capacitor of $C = 230$ pF is attached in series with the primary coil to create an LC circuit with a resonating frequency $f = (2\pi\sqrt{LC})^{-1} = 3.86$ MHz. Here, the input source is constructed using a half-bridge inverter based on GaN transistors (EPC9024). With the Litz coil, a primary current of $I = 1.5$ A is generated at the working frequency while dissipating 0.9 W of heat. This increased temperature is negligible and implies a stable operation. However, the coil made from the monolithic wire would result in higher temperatures at the primary resulting in a change in resistance and inductance values.

The fig. 4.14 illustrates the implementation of the contactless inductive heating system for the compliant SMA prototype as well as the temperature distribution across the SMA structure using the FLUKE® Ti25 thermal camera. A glass plate is placed between primary coil and the SMA to avoid any heating through convection. Using the proposed heating system, the SMA inverter prototype was heated above 120°C validating the system as an active heating system. Furthermore, as the structure reverts back to its original shape, this further validates the presence of the shape memory effect.

In this implementation of the prototype, the penetration depth does not limit the excitation frequency as the structure is composed of a thin film of SMA. In the case of a working frequency of 10 MHz, the penetration depth is larger than the 100 μm thick SMA sheet. However, in a real world application where the compliant structure is created from a thick monolithic block of SMA or 3D printed, the penetration depth would be an additional parameter to account for

when sizing the input frequency.

4.6 Designing Multi-Output Compliant SMA Actuators

The proposed design methodology consisting of using topology optimisation to design compliant SMA mechanisms was validated using a FEM simulations and experimental results using standard benchmark problems. Furthermore, as the generative design algorithm used made abstraction of the shape memory effect, the designs of the compliant mechanisms were generated with a relatively low computational time. Due to the cost of NiTiNOL and advanced manufacturing techniques, prototype of the proposed design could not be fabricated but advanced additive manufacturing methods that avoid waste of material such subtractive methods such as machining has become possible as shown in the work by citeand cite. With these techniques, complex compliant SMA actuators could be fabricated in the near future. Thus, the proposed design methodology could be a great tool in creating novel biased-spring SMA actuators.

4.6.1 Generated Multi-Output SMA Actuators

In this section, various novel multi-output actuators fabricated from compliant SMA topologies are generated based on the proposed design methodology. These topologies were, similar to the benchmark problems in section 4.4, simulated and their corresponding strain retention factors were measured, as shown in fig. 4.16. The *rhombus* structure is a multi-directional mechanism where the axes move in opposing directions. They elongate in the y-axis and contract in the x-axis. The other structures, named the 8-*point mandrel*, the 4-*point mandrel* $\times$ and the 4-*point mandrel* $+$, perform as outer-mandrels for gripping objects. The evolution of the topology during the generative optimisation process for the 4-*point mandrel* $\times$ is shown in fig. 4.15. In a similar way to the benchmark problems, these topologies are generated while making abstraction of the shape memory effect and while neglecting the nonlinear nature of the alloy so as to drastically reduce the computational time, which took less than 2 min per design.

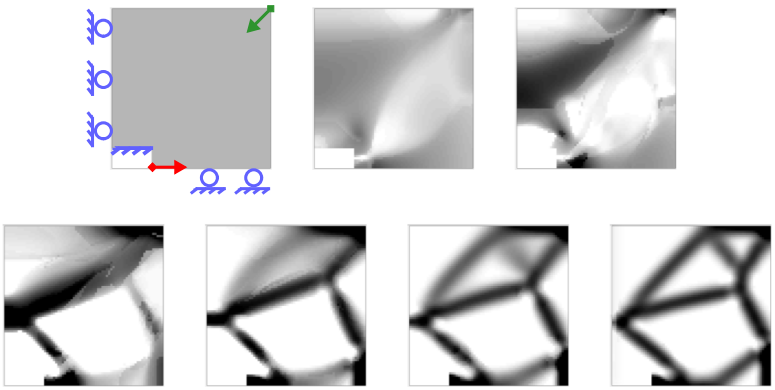

Figure 4.15: 4-point Mandrel × : Evolution throughout the optimization. The grayscale represents the value of the filtered artificial density. The input force is shown in red and the output force in green.

Using the FEM simulation of these multi-output compliant mechanisms and the strain retention factor, the presence of the shape memory effect within the generated topologies is validated. A fixed input strain of 10% is applied at each input, where the bias-spring is attached, to have comparable results for each design. The results of the FEM simulation of the design are presented in table 4.3. The obtained strain retention factor for each actuator topology shows that the majority fo the strain applied by the biasing spring is retained and will be recovered when heated using the proposed induction heating methodology. This implies that this design methodology could be an attractive tool for designing novel multi-output biased-spring SMA actuators.

4.7 Kirigami inspired Compliant SMA Actuators

Using topology optimization, various compliant SMA actuators can be designed with the intent to combine the functions of the kinematic stage and the active element. However, due to the current limitations of fabrication and its costs, the feasibility of such an actuator, in the current sense, is unlikely. As additive manufacturing of SMAs becomes more accessible, the advantages of designing compliant SMA structures such as increasing the overall work density of the actuator, will become more apparent and attractive.

Kirigami, the Japanese art of cutting paper to create intricate structure, has gained traction in various engineering fields to create stretchable structure as shown in the work by cite. While designing 3D compliant structure made of SMA is expensive, this kirigami approach can be extended to SMAs to create compliant structures that when cut in a specific manner, can exhibit surprising mechanical behaviours.

When designing actuators, a key detail to keep in mind is the life cycle of the device. In common industrial applications, the number of cycles to fatigue of traditional grippers can exceed 10^6 cycles. In the case of SMA actuators, this number is much lower and is directly

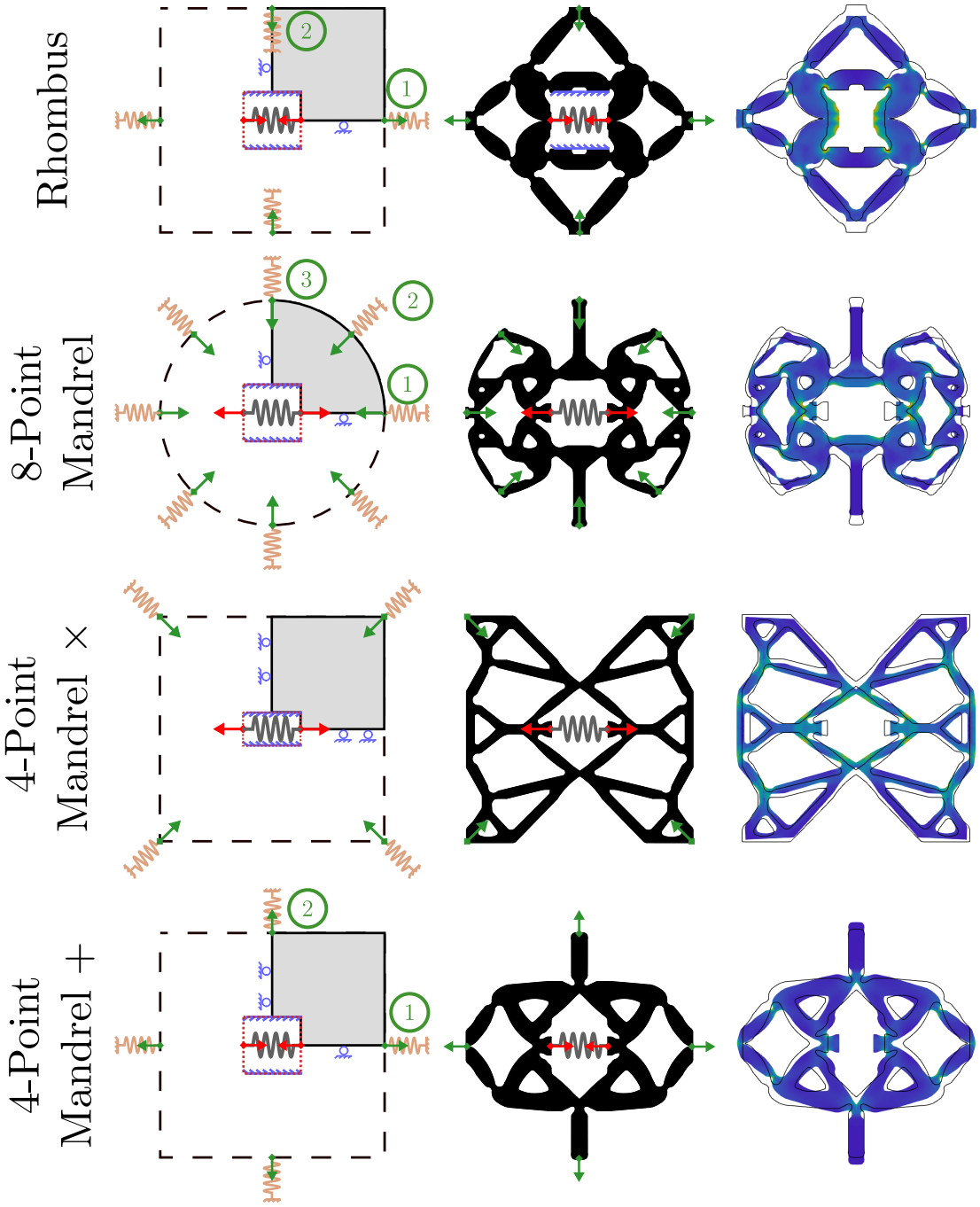

Figure 4.16: Using the novel design methodology, multi-output bias-spring SMA actuators are generated making use of compliant SMA structures, shown with normalised stress distribution in the deformed state. The input forces are shown in red and the output forces in green. The artificial springs present in the topology optimisation are shown in brown while the bias-springs of the actuators are shown in grey.

Table 4.3: Comparison between the FEM and experimental results of the modified inverter benchmark problem.

	$\varepsilon^x_{\text{loaded}}$	$\varepsilon^y_{\text{loaded}}$	$\varepsilon^x_{\text{free}}$	$\varepsilon^y_{\text{free}}$	α^x_ϵ
Rhombus	①: 0.051 ②: 0	①: 0 ②: 0.062	①: 0.042 ②: 0	①: 0 ②: 0.045	**67.9%**
8-Point Mandrel	①: -0.057 ②: -0.057 ③: 0	①: 0 ②: -0.05 ③: -0.085	①: 0.037 ②: -0.038 ③: 0	①: 0 ②: -0.034 ③: -0.058	**74.7%**
4-Point Mandrel ×	-0.029	-0.022	-0.023	-0.017	**81.4%**
4-Point Mandrel +	①: 0.051 ②: 0	①: 0 ②: 0.062	①: 0.042 ②: 0	①: 0 ②: 0.045	**68%**

related to the structural fatigue of the material. The determining factors regarding the fatigue life of SMAs are the strain amplitude and the type of strain applied to the material. The work by Runciman et al. (2011) looks at the fatigue lifetime of NiTiNOL based on different loading conditions, such as torsion, tension and bending. They conclude that SMAs tend to have a much longer life cycle when loading under torsion or bending when compared to tension. The results show that with a fixed strain amplitude of 1%, in tension, the number of cycles to failure is less than 10^3 whereas in bending or torsion, the number of cycles to failure is around 10^5.

The availability of NiTiNOL in different geometries such as springs, wires and sheets, has allowed the creation of multiple classes of SMA actuators that exploit their respective advantages. As mentioned in previous sections, the simplest approach would be to use the alloy in the shape of a wire paired with a biasing spring to drive an actuator where the stress and strain of the material corresponds directly to the stroke and force output of the actuator. In these cases, SMA wires are elongated under pure traction and are then heated to recover the strain and provide the force output as shown in the works by Kyung et al. (2008), Welsch et al. (2018), Haibin et al. (2018), and Andrianesis and Tzes (2015). Here, the stroke of the actuator can not exceed 1% without compromising its fatigue life. Thus, in cases where a larger stroke is required, the geometry of the wire is adapted to form a spring which can provide stroke above 100% as implemented in the works by Ikuta (1990) and Zhakypov et al. (2018). Here, the

material no longer deforms in traction but rather in torsion, thereby increasing its fatigue life but while compromising the force output. This implies that there is a trade-off to be made between the force output, and the stroke and fatigue life.

Since SMAs are available in the form of sheets which can be machined using laser cutters into complex geometries, different kinds of SMA actuator systems exploit the longer fatigue life of SMAs in flexion to create novel grippers as shown in the works by Kohl et al. (2002), Benard et al. (1998), Zhakypov et al. (2018). The major advantage to using sheets instead of wires is the fact that they provide a much higher force output. The difference in force output between sheets and wires can be reduced by placing multiple wires in parallel to generate forces in the same order of magnitude as sheets. Thus in applications, where a higher force output is required, the use of SMA sheets or multiple wires in parallel can be a viable solution.

When working with thin wires, placing them in parallel to augment the overall force output also increases the complexity of the system greatly. The manufacturing and assembly of such a system can be difficult. Furthermore, it is also impossible to uniformly deform all the wires equally, resulting in some wires being inactive during the shape memory effect. Thus, in cases where a higher force output is required, the design space can become limited to just using sheets. For maximum force output, the sheet can be elongated in pure traction but only up to about 1%. In applications where a large stroke and force output is required, the SMA sheets in its original state is no longer viable. Traditionally, this limitation is overcome by adding a kinematic stage to amplify the stroke of the SMA actuator but comes with the cost of reduced overall work density of the final actuator.

In this section, a novel approach will look at a new kirigami-based approach to designing SMA sheets to obtain an actuator that can provide higher force output while being able to also provide high strokes. Kirigami is a variation of origami that involves the cutting of the substrate to create different shapes and behaviours. The pattern presented in this paper is based on the work by Shyu et al. (2015) where a nanocomposite substrate is patterned to create a stretchable element. This approach allows an SMA sheet to reach strains over 100% without losing its capacity to deliver a high force output.

4.7.1 Proposed Patterns

4.7.2 Implementation

4.8 Summary and Conclusion

In this chapter, a design methodology, consisting of integrating the kinematic stage and active element to create a compact SMA actuator, is proposed. Using topology optimization and a novel approach to generate topologies while making abstraction of the shape memory effect is detailed. By implementing such a generative algorithm, the computational time to design novel topologies has been drastically reduced. This has the implication to extending such a

design algorithm to 3D structures.

The design approach using topology optimisation was tested using benchmark problems with a standard input and output parameters to create various topologies that can be fabricated from SMAs. The presence of the shape memory effect and the feasibility of the topologies to be used in SMA actuators was validated using a FEM simulation and an experimental prototype. Furthermore, a qualitative measure called the strain retention factor was proposed as a means to compare the various topologies that can be generated using such an approach.

As these novel structures can be complex, the heating of such geometries using simple Joule's heating is no longer trivial. A novel heating solution was proposed and fabricated so as to activate the shape memory effect of the fabricated topologies. Furthermore, using this design approach and generative design algorithm, various multi-output biased-spring SMA actuators, that can be actuated using only a single biasing spring, were proposed.

These SMA structures were designed within a 2D space with the intention of fabricating the structure from a 3D monolithic block of SMA. As the design algorithm was implemented with a volume constraint to preserve material, fabricating the structure with subtractive methods such as machining will result in large amounts of wasted material. However, due to the current cost limitations of additive manufacturing processes that exist for SMA, the feasibility of such a compliant SMA structure is limited.

Lastly, the same methodology where structure composed of complex patterns that exhibit surprising mechanical behaviours, can be be seen in kirigami-inspired structures. By extending this same design principle to SMA actuators, patterns can be cut into thin SMA sheets such that high stroke actuators can be fabricated without the need for cumbersome external kinematic stages.

Using this design principle, compliant SMA active elements can be designed and fabricated so as to appropriate the functions of the kinematic stage within the SMA actuator. This allows for the creation of compact SMA actuators that retain their high work energy density.

5 Integrating Control Systems into SMA Actuators

5.1 Introduction

Shape Memory Alloys, often referred to as artificial muscles, are often used in applications where a compact and lightweight solution is required. When paired with a biasing element such as a spring or compliant mechanism, a lightweight reversible actuator can be fabricated. By heating and cooling the active SMA element, a reversible back and forth motion can be created.

Due to the complex nature of the shape memory effect, sensors or complex control strategies are required for the accurate control of the SMA element, as shown in the work by citeand cite. The SMA, if overheated, can result in the permanent reprogramming of the shape or the destruction of the SMA wire or coil. In the case of smaller, more compact applications, the SMA element used are thin wires or coil. In these cases, using sensors that can measure the temperature can be quite difficult to implement due to the low thermal mass of the SMA element. Recent work such as cite, have implemented sensorless systems where the change in resistivity is measure as the SMA changes phase to create more compact control solutions. Here, due to the complex nonlinear nature of the shape memory effect requires complex control strategies and micro-controllers to efficiently control the SMA and prevent overheating.

Often, when considering the volumetric work density of SMA actuators, the electronics, sensors and control strategies are not taken into account. In certain applications, for example untethered crawling robots, the control plays an important role in the final work-weight density of the robot as seen in the work by cite. Improvements made in the sensorless and control strategies can, thus, have a major impact in the final dimensions and weight of the SMA actuator.

In this chapter, a novel design concept is presented to further integrate the discrete building blocks present in the traditional SMA actuator. By exploiting the dependence of the mechanical behaviour of the SMA and its temperature, a mechanical oscillator system can be developed

such that an electronics-free SMA actuator can be designed. This design language can be implemented into SMA actuators to create a simple but effective solution to create a sensorless, micro-controller-free control strategy that intrinsically present SMA overheating. Furthermore, in this chapter, a crawling robot is conceived using this methodology to validate this novel design approach.

5.2 Design Methodology for the Control System

As mentioned previously, due to the complex behaviour of SMAs, the sensors and control strategies required to actuate an SMA actuator can be cumbersome and reduce the overall work-weight density of the resulting robotic systems. The shape memory effect and the corresponding phase transitions are directly dependant on the temperature of the alloy. By exploiting this mechanical relationship between the temperature of SMA, the control system can be integrated into the kinematic stage, as represented in fig. 5.1.

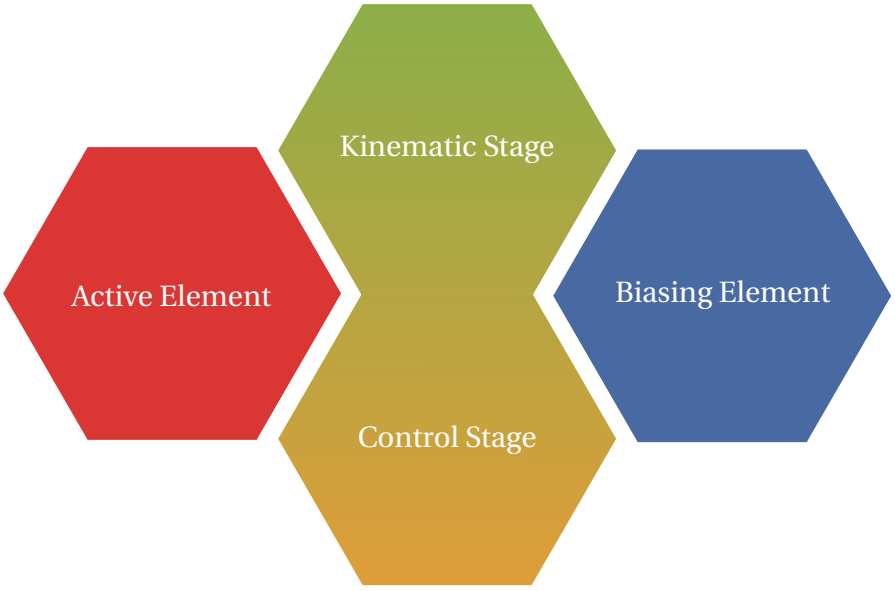

Figure 5.1: Diagram of the adapted building blocks of the SMA actuator.

5.2.1 Working principle

A basic linear SMA actuator consists of an SMA and a biasing spring that when heated and cooled, results in a simple back forth oscillating motion. By accurately controlling the temperature of the SMA above its transition temperature and below a critical overheating temperature, the SMA can be made to provide a reliable actuation. This reversible actuation results in a back and forth mechanical movement of the biasing spring and the cyclical movement of the kinematic stage, if any. The basic concept of this methodology consists of tying the mechanical behaviour of the actuator into the control.

The SMA element in most cases is heating using Joule's heating by simply passing a current through the SMA and allowing the internal resistance of the SMA element to heat up by Joule's losses as shown in the work by cite. The cooling of the SMA generally consists of passively extracting the heat from the active element using natural convection with the cooler surrounding air. This simple strategy is often used in the control of SMA actuators due to not requiring any additional mechanisms and thus, does not reduce the work-density of the actuator while keeping the system compact.

Thus, by using the mechanical behaviour of the actuator to cut the current flow across the SMA will immediately cool the active element before it has a chance to overheat. In this manner, the control of the SMA actuator is mechanical controlled by the shape memory effect. Here, as a current is passed through the SMA wire or coil, it heats up the SMA resulting in a strain recovery and the SMA returning to its original length. This change in length, after a certain threshold, can be made to physically cut the electrical contact between the SMA element and the power supply. This cause the immediate cooling of the SMA through heat exchange with the surrounding air. As the SMA cools down, the biasing element will, once again, deform the SMA which will re-establish the electrical contact across the SMA, restarting the oscillating motion. Thus, this design strategy when integrated into the kinematic stage can render the entire SMA actuator compact and electronics-free.

This approach, when properly implemented, can result in an robotic system where a reversible actuation can be observed without the need for any electronics, micro-controllers or sensors, preserving the work-weight density of the system. A mechanical control of the SMA element can result in a system where the SMA element, due to the physical electrical contacts being interrupted, can never overheat.

5.2.2 Implementation

The basic implementation of such as system consists of using a latch system or multi-stable mechanism where after a certain stroke or force threshold results in a snap-through effect that can be exploited to disconnect the electrical contacts across the SMA wire or coil. The rapid bifurcation or spring back from a latch system is used to cut the flow of current across from the SMA and the slow return of the SMA actuator due to cooling can be used to re-establish the electrical connection to create this oscillating effect.

The implementation of this oscillator mechanism in the scope of a simple biased-spring SMA actuator consists of a magnetic or mechanical latch system. A diagram of the working principle of the proof-of-concept can be in fig. 5.2. The latch, here, consists of a magnet mounted on a leaf spring that is attracted to the end-effector of the bias-spring SMA actuator. The electrical current, in this case, is made to flow across the conductive magnet and into the SMA coil. Thus, only as the the magnet attaches to the end-effector of the SMA actuator will the SMA coil be heated using Joule's losses. Essentially, as the magnet and the SMA coil makes contact, the SMA element is heated and reduces in size due to the shape memory effect. During this

phase, the magnet, which is mounted to a leaf spring, experiences a return force, F_S, and will continue to follow the actuator. Once, this force exceeds the attractive magnetic force, F_{mag}, between the magnet and the SMA coil, the latch detaches and immediately returns to its original location. This spring back occurs due to the resting return force of the leaf spring attached to the magnet. This concept can be implement in numerous ways including a mechanical latch mounted on a passive spring. Once this snap-through occurs, the electrical connection and the electrical current across the SMA is cut and will only be re-established when the bias spring of the SMA deforms the SMA coil and extends it back towards the latch. In this manner, the oscillating behaviour is observed without any sensors, micro-controllers or electronics.

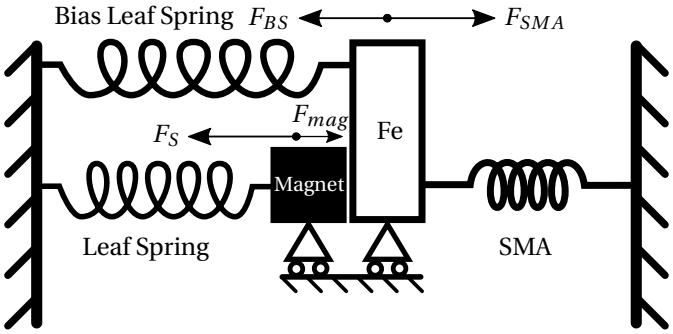

Figure 5.2: Diagram showing the working principle of the magnetic latch system implemented in the SMA oscillator.

As mentioned earlier, using a flexure-based mechanism permits the omission of a dedicated spring in the design. As seen in fig. 5.3, a proof-of-concept of this design methodology is implemented. Here, the linear stage is comprised of two parallel cantilever beams that also behaves as leaf springs. These biasing leaf springs apply a tractional return force on the SMA coil at a lower temperature while also preventing any unwanted degrees of freedom in the other axis. Another leaf spring is used to apply the return spring force required in the magnetic latch. Here, the SMA actuator is heated using the magnetic latch system and the snap-through of the latch occurs when the return force of the leaf spring exceeds the attractive force of the magnet, $F_S > F_{mag}$. Therefore, the required contraction of the SMA coil, ε, can be controlled by sizing the leaf spring associated with the magnet.

$$\varepsilon = \frac{F_{mag}}{K_s} \tag{5.1}$$

where K_s is the rigidity of the leaf spring which depends on the dimensions of the cantilever beams and can be calculated using the analytical model described in the works by Rubbert et al. (2016) and Henein et al. (1998).

Here, in this proof-of-concept, the magnetic latch consists of a small magnet, with an attractive force of 150 g, mounted on a thin leaf spring measuring 500μm × 2.5mm × 30mm. An M2 screw is used to clamp an electrically conductive wire to the magnet and acts as the ground

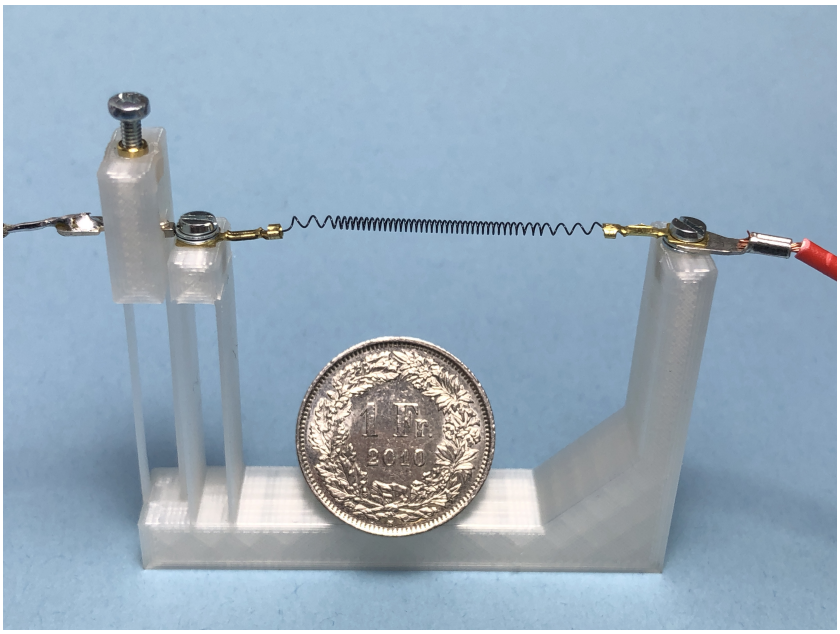

Figure 5.3: The integrated SMA control system implemented using a flexure-based magnetic latch creating an SMA mechanical oscillator.

of the electrical circuit. The magnet latches onto another ferromagnetic M2 screw which is mounted to the end-effector of the SMA actuator, as seen in fig. 5.4. The SMA is supplied by *Dynalloy, Inc* (Irvine, CA) and is a 90°C Flexinol® coil with wire diameter of 200 μm and an outer diameter of 1.4 mm. The coil contains around 40 coils and with a solid length of 8 mm. The SMA is mounted on a 3D printed support containing a flexure-based linear stage which supports the free end of the SMA. The linear stage is 3D printed from PLA and consists of 2 parallel leaf springs with dimensions 500 μm x 10 mm x 30 mm.

This basic concept can be implemented in using different methods. The latch system can be replaced by a bistable mechanism and can then be paired with antagonistic SMA actuators. Here, the control system can be linked to the snap-through of the bistable mechanism where each stable position controls the heating of each SMA element. In this way, the first SMA can be heated till the snap-through of the bistable mechanism which will then change the electrical contact across the antagonistic SMA. This concept has been implemented and validated in section 6.3.

5.2.3 Sizing of the oscillator

As mentioned previously, the thermomechanical behaviour of the SME is exploited to create the mechanical control system. The sizing of the oscillator system is, thus, directly, dependant on the thermal properties of the active element. The rise time or time till the snap-through occurs, depends on the time required to heat the SMA using Joule's heating. This implies that the current supplied across the SMA dictates the rise time of the oscillator. The fall time or

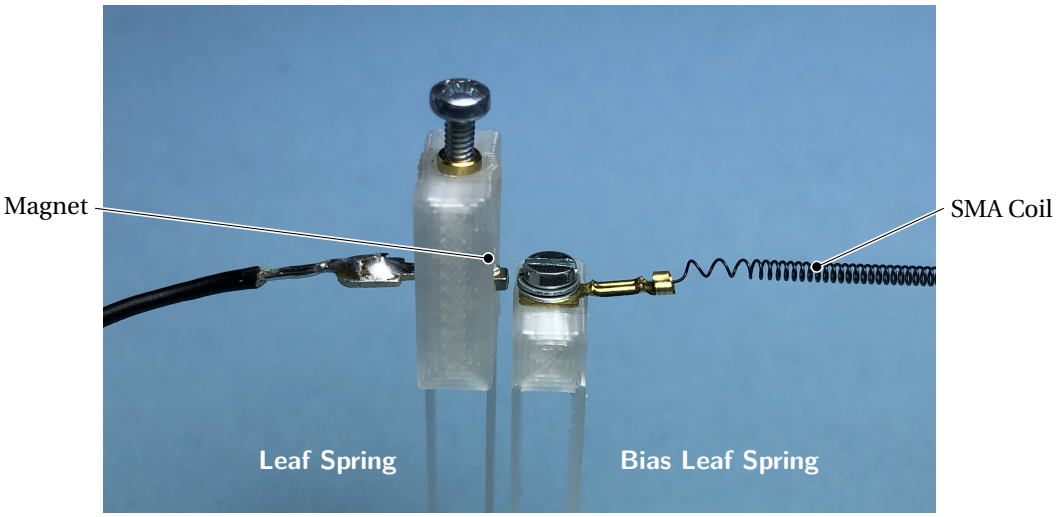

Figure 5.4: The close-up structure of the magnetic latch system that acts as the oscillating electrical contact for the SMA coil. Here, the biasing leaf spring also act as a linear stage for the actuator.

time required to re-establish the electrical contact across the SMA depends on the cooling time of the SMA wire or coil. In the case where the SMA is cooled using passive thermal exchange with the surrounding air, the fall time can be controlled by adequately sizing the diameter of the SMA wire or coil. The amplitude of the system, in this case, depends on the latch system and can be sized using the equation 5.1. Furthermore, the stroke of the SMA actuator can be sized using the methods presented in chapter 3 so as to ensure that the actuator is capable of deforming to the levels demanded by the oscillator amplitude. This will ensure that the snap-through of the oscillator occurs before the SMA overheats.

The fall time of the control system can be calculated using a simple thermal model based on the passive cooling of the SMA wire or coil. Here, the time constant, τ_c, of the system in which the thermal exchange of heat from the surface of the SMA to the surround air is used to cool down the SMA can be expressed as :

$$\tau_c = \rho c d/(kH) \tag{5.2}$$

where ρ [kg/m^3] is the density, c [J/(kgK)] is the specific heat capacity, d is the wire diameter, $k = 4$ is the ratio between the surface area of heat exchange, A_S and the volume of the active element, V, and H [W/(m^{2}K)] is the heat transfer coefficient. The thermal model of the wire can be expressed as :

$$T(t) = T_R + (T_2 - T_R)e^{-t/\tau} \tag{5.3}$$

where T_R is the ambient room temperature and t is time. Thus, the cooling time, t_c, based on

the temperature gradient between the SMA and the surrounding air, can be expressed as :

$$t_c = \tau_c \log \frac{T_2 - T_R + \frac{T_2 - T_1}{2}}{T_2 - T_R - \frac{T_2 - T_1}{2}} \tag{5.4}$$

where the subscripts, 1 and 2, represents the operating points of the actuator as shown in chapter 3. The physical properties of the SMA were obtained by consulting the data given by the supplier at *Dynalloy*.

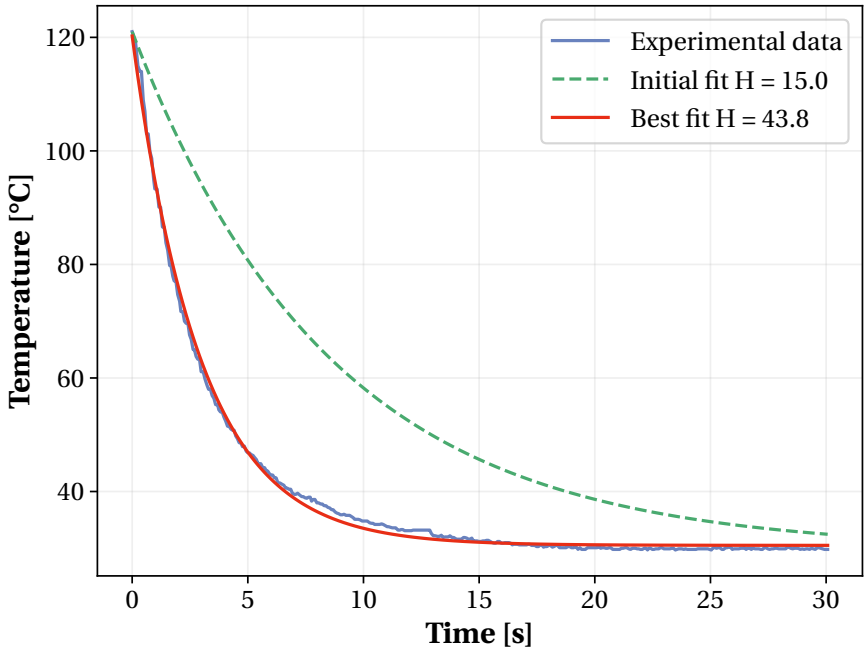

Figure 5.5: Measurement of the heat transfer coefficient, H, using 250 μm wire diameter SMA spring with a mandrel size of 0.5 mm.

Using a thermal camera with an optical zoom that allows for high spatial resolution and using equation 5.3, least-squares minimization is used to fit this thermal model to the cooling time of an SMA coil of 250 μm wire diameter. By doing so, the heat transfer coefficient, H, can be estimated. Using the model and the estimated parameters, the time constant and cooling times of other diameter SMA springs can be extrapolated. By extrapolating the cooling times of different diameter SMA springs, these values can be used to size this oscillator control system for other applications. In fig. 5.6, the cooling based on wire diameter of different SMA springs can be seen. Using these values, the fall time of the oscillator can be estimated for any wire diameter.

The rise time of the oscillator, t_h, can be estimated by calculating the time required to heat the SMA wire using Joule heating. Using the known resistance of the SMA wire, R, and the current, I, supplied to the system the heating time can be easily measured using the basic laws of electro-thermodynamics. In the case of slower rise time with small currents, the loss of

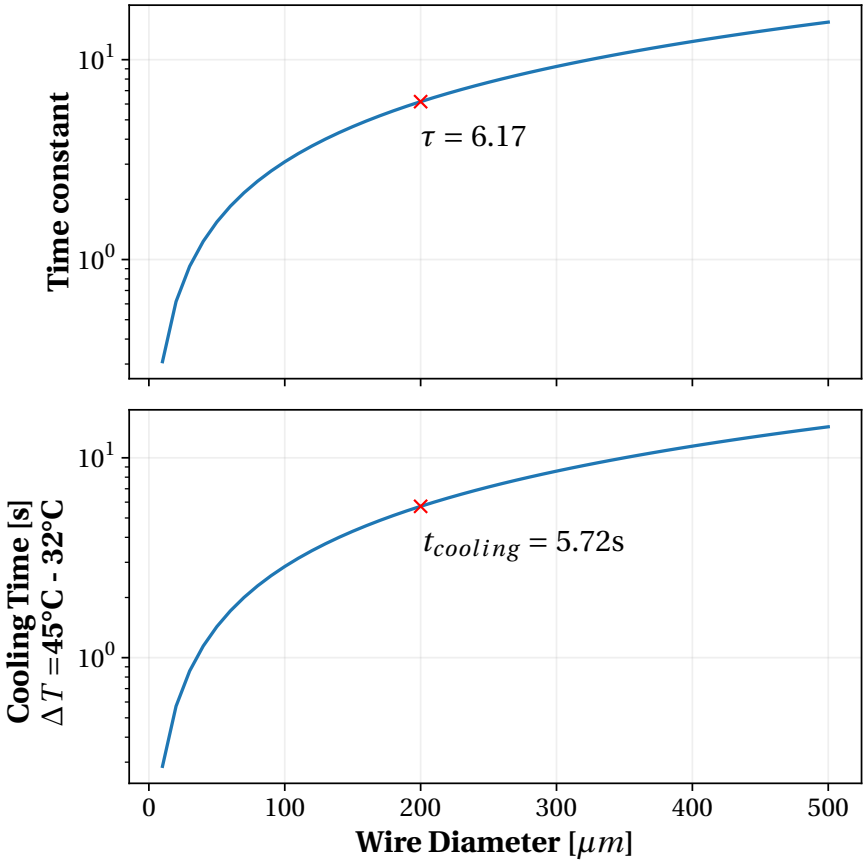

Figure 5.6: Extrapolation of the cooling time based on wire diameter with $H = 43.8$ W/(m^{2}K).

heat with the surrounding air by convection must be taken into account and can be estimated with the equation :

$$t_h = \int_{T_1}^{T_2} \frac{\rho V c}{I^2 R(T) - H A_S (T - T_R)} dT \tag{5.5}$$

The control system was supplied with a constant current and left to oscillate for 2 minutes to test the repeatability and consistency of the rise and fall times. The temperature of the SMA coil was measured using a thermal camera with high spatial resolution and the stroke of the SMA actuator was measured using a laser displacement sensor. In fig. 5.7, the temperature and position fluctuations of the oscillator are shown. The rise time of the magnetic latch-based control system when supplied with 340 mA was measured to be 3.8 ± 0.18 s while the rise time when supplied with 840 mA was measured to be 0.64 ± 0.09 s. The cooling time when supplied with 340 mA and 840 mA was found to be 5.71 ± 0.09 s and 5.82 ± 0.2 s, respectively. Thus, the period of the oscillations for the two measurements were found to be 9.60 ± 0.17 s and 6.47 ± 0.22 s which corresponds to a frequency of 0.10 Hz and 0.16 Hz.

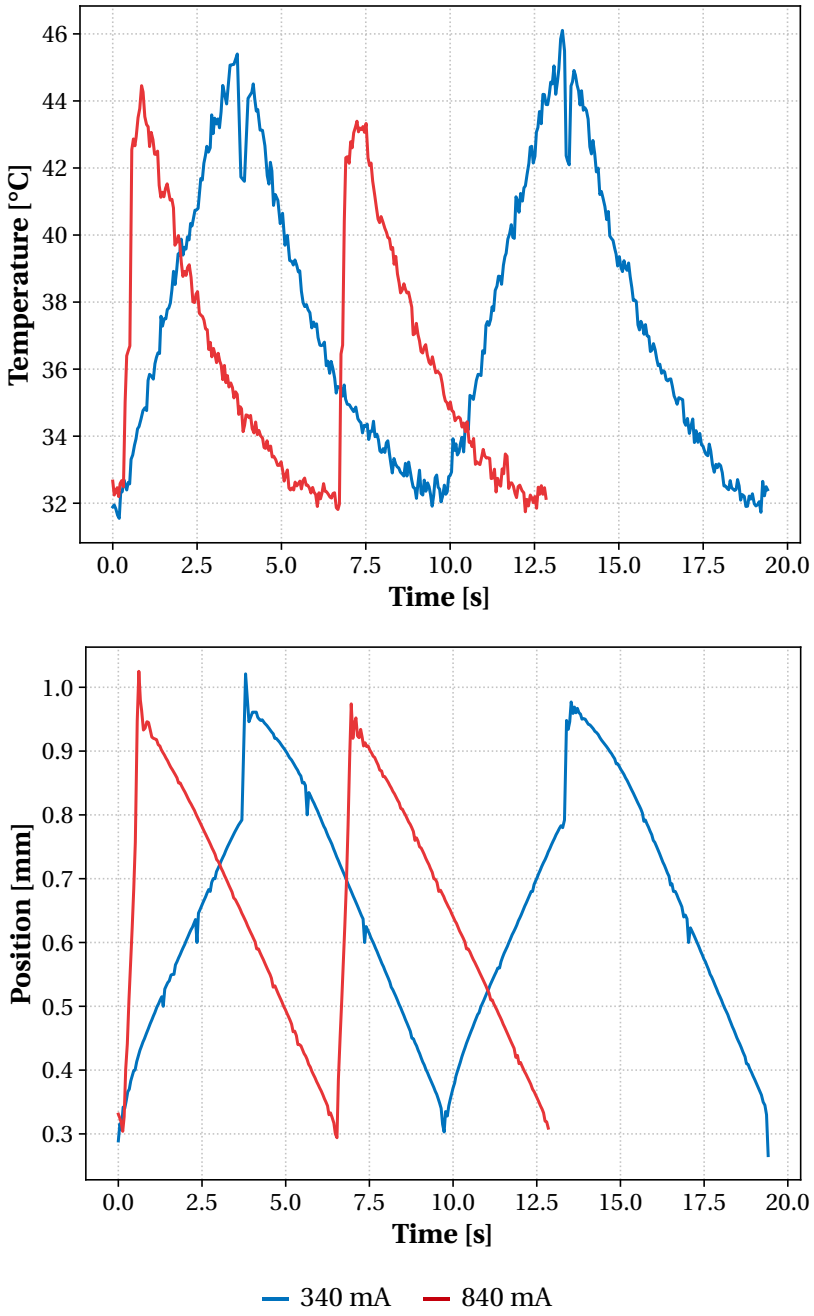

Figure 5.7: Effect of the current on the evolution of the SMA spring's temperature and position.

The rise time and cooling times of the latch-based control system were measured by detecting the peaks and troughs of the measured signals. The mean and standard deviation of these values were then calculated. Furthermore, the cooling time predicted, in fig. 5.6, based on the SMA geometry corresponds to the measured values, thus, validating the thermal model. Also, the cooling time remains relatively constant with respect to the varying current across the SMA. The cooling times can, thus, be predicted using the analytical model and the value

remains constant, even while varying the current. This implies that the control system can be sized for a fixed fall time by appropriately sizing the SMA wire diameter.

This magnetic latch system allowed the bias-spring SMA actuator to be actuated without any sensors or risk of overheating the SMA. The latch was required to allow the SMA to be heated during the entire stroke of the latch. A system using pogo pins, which are electric contacts consisting of a plunger and a spring mounted inside a barrel, was also tested. This resulted in a behaviour where the bias-spring SMA actuator oscillated at the tip of the pin. This, unfortunately, showcased the need for a latch system to bring the electric contact back to the starting position such that the actuator can carry out its entire stroke during the cooling phase. A latch system based on friction and snap-fits can be designed as an alternative. This pogo pin solution had the unexpected effect of allowing the SMA coil to be maintained at a stable temperature. This effect could be potentially used to stabilise an SMA at a fixed temperature based on the stroke of the pogo pin. The behaviour was not further explored in this paper.

5.3 Validation of the Approach using a Case Study

As stated previously, the requirement of sensors and complex control strategies in certain applications were compactness and being lightweight are required, pollute the overall work-weight density of the robotic system. In this section, to validate the novel design methodology for mechanical control solutions, a lightweight and compact crawling robot powered by shape memory alloys is designed and fabricated. Here, in the creation of an untethered crawling robot, the presence of sensors or micro-controllers will play an important role in the final work density of the system.

In this SMA driven crawling robot, the magnetic latch-based control system is implemented so as to create a small scale robot that can be driven without any sensors or electronics. In this mechanism, the high work density of the SMA is not compromised due to the lack of large biasing-springs and control electronics when compared to examples such as the work by cite.

5.3.1 Background and Biological Analysis

The mobile robot fabricated using this design approach is inspired by the gait of the inchworm. This insect is not a type of worm but in-fact, a type of caterpillar. These inchworms are known for their peculiar type of locomotion made possible by a looping motion called the two-anchor crawling gait, as described in the work by cite. Its gait consists of attaching its forelegs and using the muscles located in its abdomen to pull the rest of its body, as demonstrated in cite.

The gait, as seen in cite, consists of alternating between gripping or slipping against the ground. Initially, the forelegs are made to slip while the abdominal muscles push against the hing-legs which are now planted firmly on the ground. Nest, the forelegs are made to grip the ground and the abdominal muscles pull the rest of the body while the hind-legs slide across

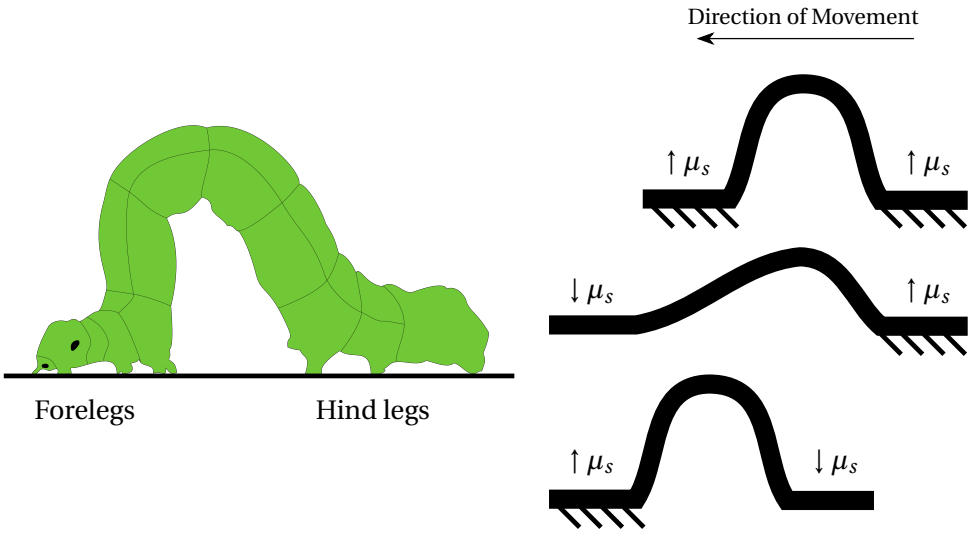

Figure 5.8: The gait analysis of an inchworm showing the insect change the coefficient of friction (μ_s) with respect to the ground by either gripping or sliding its legs.

the ground. This pattern is repeating to allow the inchworm to crawl across the surface. The presented mobile robot exploits this gait to create a similar crawling locomotion.

5.3.2 Working principle and Implementation of the Robot

The basic working principle of this mobile robots consists of implementing the design methodology presented in chapter 3 and the magnetic latch-based control system. Here, the linear movement of the SMA oscillator is transformed into a rotation of a pair of legs such that the tips or claws of the leg pulls the body of the insect robot across the ground.

As seen in fig. 5.9, the inchworm robot is entirely 3D printed in a single piece and is powered using an SMA coil. The control system used in this design is based on the approach detailed in section 5.2.2. The legs of the insect robot is attached to the end-effector of the SMA actuator so as to harness the strain recovery when the SMA coil is heated using Joule's heating. Here, as detailed in chapter 3, the biasing element of the SMA actuator consists of a flexure-based cantilever leaf spring. This biasing element also acts as a simple kinematic stage that transforms the SMA linear strain recovery into a rotation of the robot legs.

The insect robot operates in a similar manner to the inchworm presented in section 5.3.1 where the claws alternate between high friction and low friction with respect to the ground. By activating its artificial abdominal muscle consisting of the SMA coil, the insect robot is able to crawl across the ground. Here, the alternating friction that occurs at the claws is due to the design of the tips of the insect legs. The angle of the legs as the robot moves changes the angle of contact with the ground surface. As the leg tip design is asymmetrical with the direction of movement, the rotation of the legs cause alternating high and low friction. The behaviour is similar to a ratchet system where one degree of freedom is allowed in the forward direction but

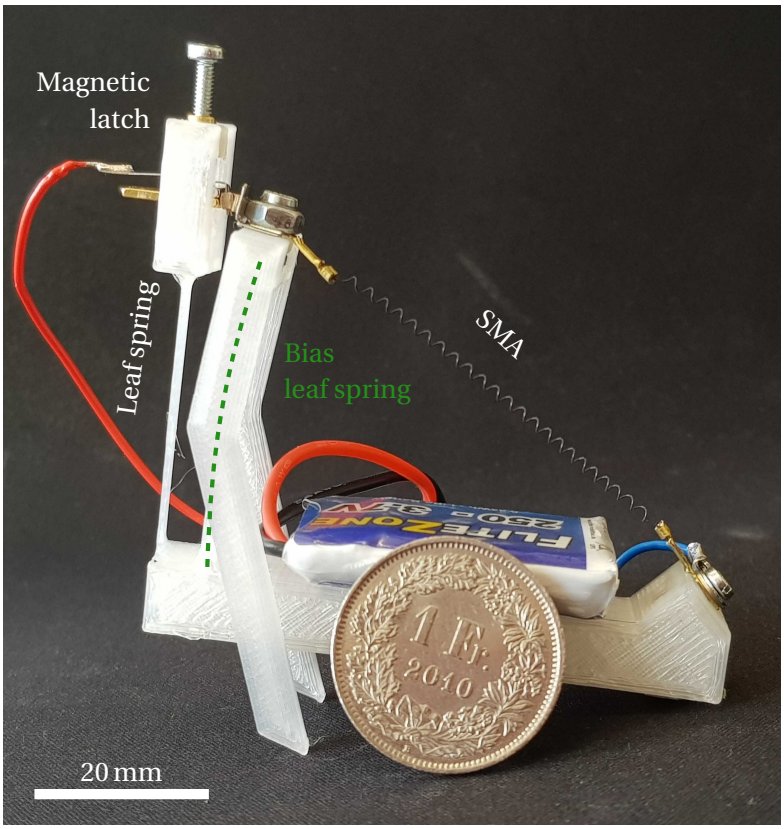

Figure 5.9: The implementation of the insect robot around the mechanical SMA oscillator.

not in the backward direction. Here, the claw design allows rotation in the clockwise direction but prevents some rotation in the anti-clockwise direction. As the SMA is heated, the insect robot moves its forelegs away from the body. Then, when the SMA coil is stretch by the biasing leaf spring during cooling, the forelegs grip the ground and drags the rest of the body along the ground. By repeatedly heating and cooling the SMA, the insect robot can gradually move across the ground. As detailed in this novel control strategy, the magnetic latch system allows the SMA to oscillate and control the steps of the insect robot without any micro-controllers or electronics.

5.3.3 Analytical model of the Biasing Compliant Mechanism

When sizing the design and SMA of the insect robot, an analytical model of the compliant mechanism is required. This models allows dimensioning the SMA coil such that sufficient stroke is observed during the shape memory effect. Here, the stroke of the SMA actuator or the contraction of the SMA coil corresponds to the estimated step length of the insect robot.

The crux of the design revolves around the flexure-based biasing element and kinematic stage which, in this design, consists of a simple cantilever leaf spring. This flexural structure converts the linear contraction of the SMA coil into the rotation of the insect legs while also serving as

the bias spring for SMA actuator allowing the coil to be stretched during the cooling phase based on the design approach detailed in chapter 3.

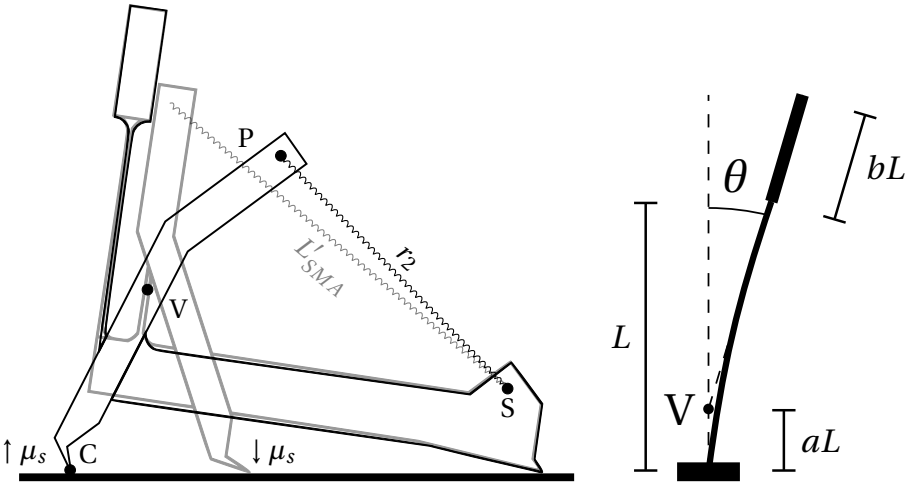

Figure 5.10: The working principle of the insect robot showing the simplification of the cantilever beam to a virtual rigid body pivot. The claw design changes the coefficient of friction (μ_s) of the insect with respect to the ground allowing the robot to crawl.

The pseudo-rigid-body model, as described in the work by Howell et al. (2013), is used to model flexure-based mechanisms such as the cantilever beam as traditional rigid-body mechanisms. Thus, by simplifying the cantilever leaf spring as a virtual pivot, an analytical model can be established to estimate the effect of the SMA coil contraction. In the work by Zhang et al. (2007), the location of the virtual pivot can be estimated with relative accuracy to a point at a distance of aL from the clamped end of the cantilever beam, where L is the length of the beam, bL is the length of the rigid attachment point with the SMA coil and a is:

$$a = \frac{1+3b}{3+6b} \tag{5.6}$$

The pre-stretched SMA coil of length, L'_{SMA}, is attached to the biasing cantilever leaf spring at the free end as shown in fig. 5.10. The position of cantilever tip, $P(x_P, y_P)$, as the SMA coil contracts in length by ε, can be deduced by finding the intersection between the two circles with radii, r_1 and r_2, and with centres at the virtual pivot $V(x_V, y_V)$ and fixed end of the SMA coil $S(x_S, y_S)$, respectively.

$$P(x,y) = \frac{1}{2}\begin{pmatrix} x_V + x_S \\ y_V + y_S \end{pmatrix} + \frac{r_1^2 - r_2^2}{2R^2}\begin{pmatrix} x_S - x_V \\ y_S - y_V \end{pmatrix} \pm \frac{1}{2}\sqrt{2\frac{r_1^2 + r_2^2}{R^2} - \frac{(r_1^2 - r_2^2)^2}{R^4} - 1}\begin{pmatrix} y_S - y_V \\ x_V - x_S \end{pmatrix} \tag{5.7}$$

where R is the Euclidean distance, $|\overline{VS}|$, between the two circle centres, $r_1 = (1 - a + b)L$ and

$r_2 = L'_{SMA} - \varepsilon$ representing the current length of the SMA coil.

As the insect legs are attached at the cantilever tip, the claw tips, $C(x_C, y_C)$, of the insect robot can be estimated by using a series of simple translation and rotation transformations from the cantilever tip based on the angles (α) and lengths (L) of the insect leg segments.

$$C(x,y) = \begin{pmatrix} x_P \\ y_P \end{pmatrix} + \sum_{i=1} L_i \begin{pmatrix} \cos(-\frac{\pi}{2} - \theta + \sum_{i=1} \alpha_i) \\ \sin(-\frac{\pi}{2} - \theta + \sum_{i=1} \alpha_i) \end{pmatrix} \tag{5.8}$$

Thus, based on the contraction or strain recovery of the SMA coil (ε), the step length of the insect, ΔC, can be estimated by taking the Euclidean distance between the claw tip location before and after the SMA contraction. The position of the insect robot claw and the step length based on the SMA coil contraction can be seen in fig. 5.11.

5.3.4 Implications of the Prototype

As detailed in the methodology, the analytical model of the inchworm robot that determines the relationship between the contraction of the SMA during actuation and the estimated step length was first estimated. This design was simulated using a commercial finite element modelling (FEM) software which was then used to validate the analytical model, as shown in fig. 5.11. Furthermore, the experimental results obtained from the inchworm prototype was used to validate the model, as shown in the same figure. This comparison shows that the pseudo-rigid body model used to model the design is quite accurate and can thus be used to further optimize the step length in future iterations.

Table 5.1: The design parameters of the inchworm robot.

Parameter	Value
SMA dimensions	Coil: ∅1.37 × 12 mm Wire: ∅0.2 mm
Biasing Leaf Spring	30 × 10 × 0.6 mm
Magnet Leaf Spring	30 × 2.5 × 0.6 mm
Magnet force	250 g
Battery Life	1.6 min @ 20 mAh

Due to the design being based on flexure-based structure, the inchworm could be fabricated from a single 3D printed piece. The structure was printed from PLA filament using fused deposition fabrication based on the parameters shown in table 5.1. Due to the novel control system based on the magnetic latch, when connecting the robot to a 20 mAh battery, the robot

is able to crawl untethered , as shown in fig. 5.12, for an estimated 1.6 min. When allowed to crawl on a flat surface, the average speed of the insect robot was measured to be 1.55 mms^{-1}, as shown in fig. 5.13. The efficiency of the leg design is highly dependant on the surface; smoother surfaces cause the legs to slip and drastically changes the overall efficiency of the design.

As stated, the principle advantage to the novel control system approach is the absence of sensors or micro-controllers. Using this methodology, the total weight of the robot including the battery weights 9.7 g. The insect robot is powered using only a single SMA coil. As with most SMA actuators, the coil is heated using Joule's heating by passing a current through it. Here, the heating consists of passing a 770 mA current for a duration of 750 ms with a power of 1.7 W. As shown in fig. 5.11, the step length of the insect robot was measured to be 8 mm.

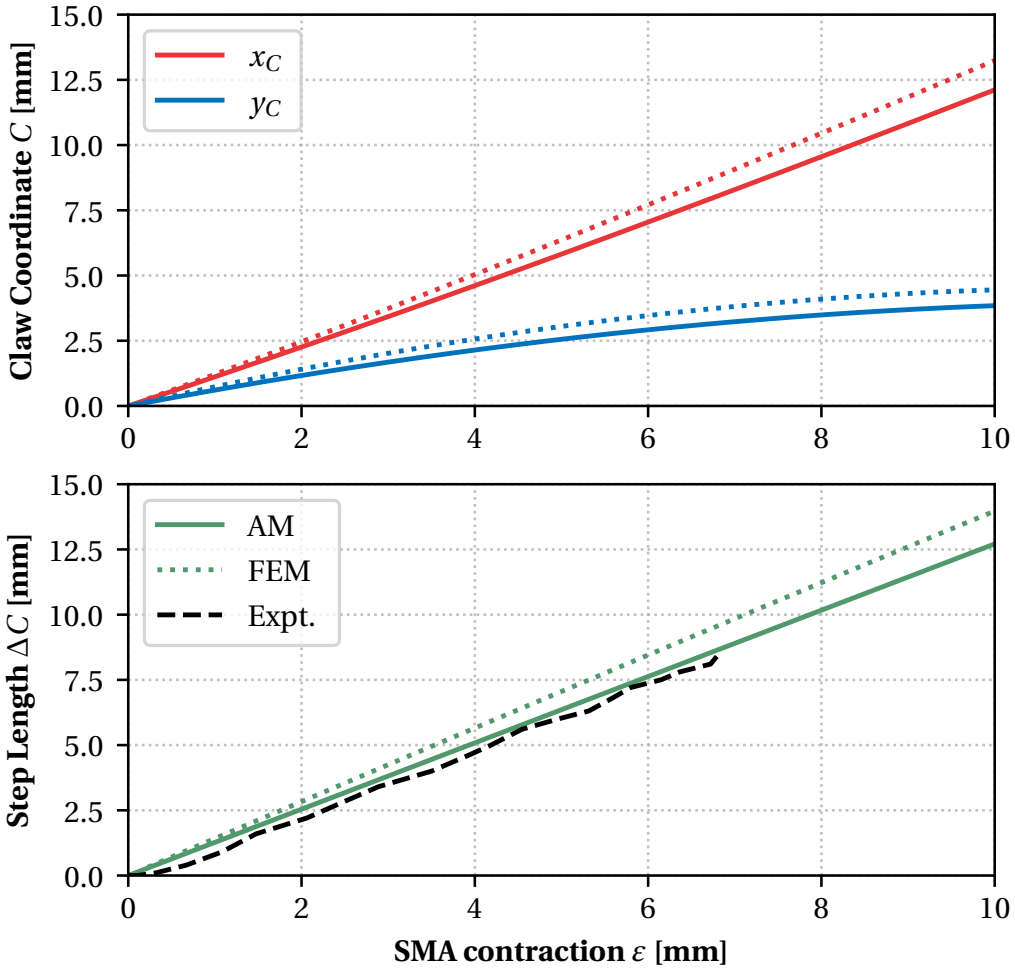

Figure 5.11: Comparison of the leg tip displacement versus the contraction of the SMA coil between the analytical model (AM) and Finite Element Model (FEM) simulation. Here, the dotted and filled lines represent the FEM results and analytical model, respectively.

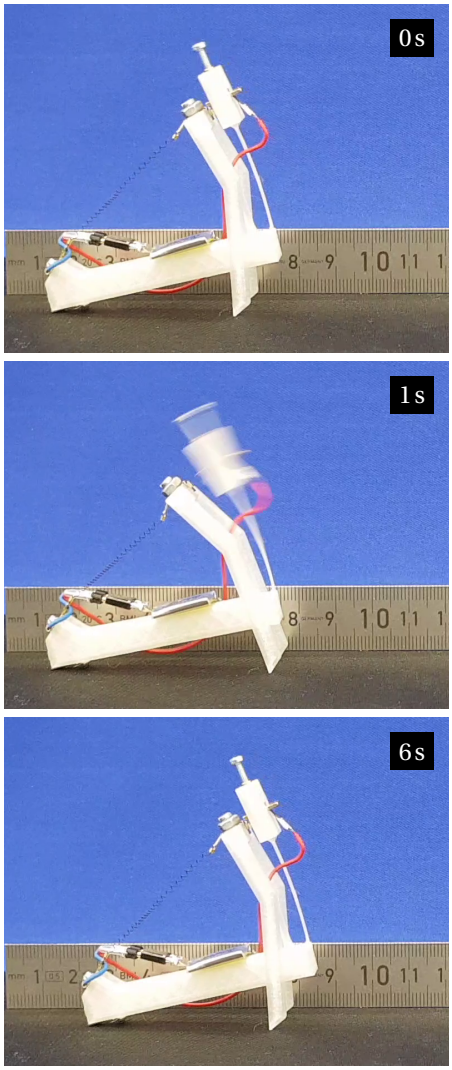

Figure 5.12: The untethered gait of the insect robot with a step length of 8.4 mm. As predicted, the snap-through of the magnetic latch halts the heating of the SMA coil.

Often, in the case of mobile robots, especially bio-inspired robots, the cost of transport (CoT) is calculated to compare the design and implementation. This factor allows the comparison of mobile robots with varying structures, sizes and gaits. It can be calculated using the following equation :

$$\text{CoT} = \frac{E}{mgd} \tag{5.9}$$

where E is the energy required to heat the SMA, m is the total mass of the robot including the battery, g is the acceleration due to gravity and d is the step length of the robot. Using the equation, the CoT was calculated to be around 1620 $\text{Jkg}^{-1}\text{m}^{-1}$. This is comparable to other untethered inchworm robots like in the work by Ji et al. (2019) whose CoT is measured to be 1670 $\text{Jkg}^{-1}\text{m}^{-1}$. However, when compared to other inchworm robots, as shown in table 5.2,

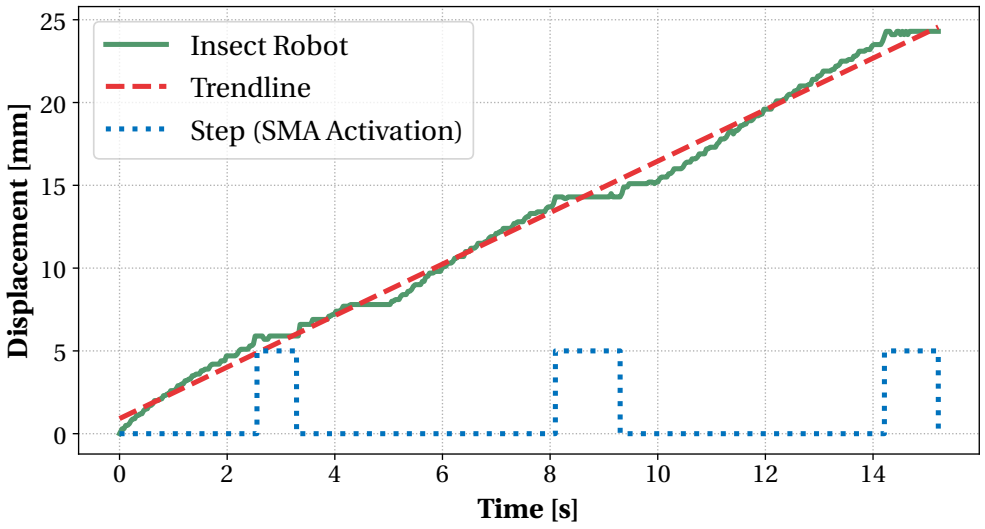

Figure 5.13: The displacement of the insect robot. The average speed of the robot is 1.55 mms^{-1}. Here, the step line represents the state of the SMA. A high value denotes that the SMA coil is being heated and a low state denotes that the SMA coil is cooling down.

this work is limited in the overall speed. This can be explained due to the inefficiency in the claw design and the dependence on the friction with the ground. The design, while being cheap and easily fabricated using 3D printing, it is limited by the PLA material. By optimizing the material to create thinner leaf springs, the size of the robot can be greatly reduced. Future work will have to include the optimization of the claw design and improve the overall efficiency of the insect robot's claw design to prevent slipping.

5.4 Summary and Conclusion

In this chapter, a novel approach to design a mechanical control system is presented. In this methodology, the control stage of a traditional SMA actuator is integrated into the kinematic stage of the actuator. This results in a control mechanism that uses the thermomechanical behaviour of the SMA such that the system no longer requires any sensors or electronics.

Furthermore, a basic implementation of such a system is presented using a magnetic latch-based system. Using a magnet and flexure-based cantilever leaf springs, a magnetic latch was designed and implemented where after a certain stroke threshold, results in an instantaneous snap-through. This rapid bifurcation is exploited to instantly disconnect mechanically the electrical contact across the SMA and thus, preventing any overheating. This design principle was implemented by fabricating a basic SMA mechanical oscillator that requires no sensors or electronics to oscillate.

Lastly, the design methodology was validated using a case study consisting of an untethered crawling insect robot powered by a single SMA coil. Here, based on the presented design

Table 5.2: Comparison of various different smart material based mobile robots using data from the work by Ji et al. (2019)

Smart Material Technology	Robot length (BL) [mm]	Speed [mms^{-1}]	Speed [BLs^{-1}]	Total weight [g]	Speed / weight [BLs^{-1} per g]
SMA [This work]	60	1.55	0.03	9.7	0.003
SMA [Koh and Cho (2013)]	150	10	0.07	1.2	0.055
SMA [Huang et al. (2018)]	57	34	0.6	~20	0.03
DEA [Ji et al. (2019)]	40	12	0.3	0.97	0.3
DEA [Cao et al. (2018)]	200	4	0.02	252.6	8×10^{-5}
Pneumatic actuator [Tolley et al. (2014)]	650	5	0.008	~4000	2×10^{-6}
IPMC [Must et al. (2015)]	45	0.45	0.01	0.83	0.01

methodology, a biasing flexure-based SMA actuator was modelled and sized to power the crawling robot. Furthermore, the control system presented in this chapter, was implement using the magnetic latch system so as to create a reversible control scheme for the SMA actuator. The kinematic stage, which acts as the biasing element of the SMA actuator, is exploited within the control system. Based on the results from the locomotion of the insect robot, a regular step size and walking speed is observed, thus, validating the design approach presenting in this chapter.

Using the methodology presented in this chapter, a novel control system can be designed and sized such that the SMA actuator can be controlled without the need for bulky sensors and micro-controllers and without the risk of overheating the SMA element.

6 Validation using Novel SMA Gripper Systems

In this final chapter, the novel design methodology is validated using 3 different case studies. These case studies employ the strategies and analytical models presented in chapter 3. While validating the different analytical models, these case studies also validate the basic premise of the methodology.

6.1 Introduction

6.2 Case Study: A Multi-Output SMA Mandrel

6.3 Case Study: A Bistable SMA Gripper

6.4 Conclusion

Conclusion

A An appendix

Lorem ipsum dolor sit amet, consectetuer adipiscing elit. Ut purus elit, vestibulum ut, placerat ac, adipiscing vitae, felis. Curabitur dictum gravida mauris. Nam arcu libero, nonummy eget, consectetuer id, vulputate a, magna. Donec vehicula augue eu neque. Pellentesque habitant morbi tristique senectus et netus et malesuada fames ac turpis egestas. Mauris ut leo. Cras viverra metus rhoncus sem. Nulla et lectus vestibulum urna fringilla ultrices. Phasellus eu tellus sit amet tortor gravida placerat. Integer sapien est, iaculis in, pretium quis, viverra ac, nunc. Praesent eget sem vel leo ultrices bibendum. Aenean faucibus. Morbi dolor nulla, malesuada eu, pulvinar at, mollis ac, nulla. Curabitur auctor semper nulla. Donec varius orci eget risus. Duis nibh mi, congue eu, accumsan eleifend, sagittis quis, diam. Duis eget orci sit amet orci dignissim rutrum.

Bibliography

Alonso, C., Ansola, R., and Querin, O. M. (2014). Topology synthesis of Multi-Input–Multi-Output compliant mechanisms. *Advances in Engineering Software*, 76:125–132.

Andrianesis, K. and Tzes, A. (2015). Development and Control of a Multifunctional Prosthetic Hand with Shape Memory Alloy Actuators. *Journal of Intelligent & Robotic Systems*, 78(2):257–289.

Benard, W. L., Kahn, H., Heuer, A. H., and Huff, M. A. (1998). Thin-film shape-memory alloy actuated micropumps. *Journal of Microelectromechanical Systems*, 7(2):245–251.

Bendsoe, M. P. and Sigmund, O. (2013). *Topology Optimization: Theory, Methods, and Applications*. Springer Science & Business Media. Google-Books-ID: ZCjsCAAAQBAJ.

Cao, J., Qin, L., Liu, J., Ren, Q., Foo, C. C., Wang, H., Lee, H. P., and Zhu, J. (2018). Untethered soft robot capable of stable locomotion using soft electrostatic actuators. *Extreme Mechanics Letters*, 21:9–16.

Chouinard, P. and Plante, J. (2012). Bistable Antagonistic Dielectric Elastomer Actuators for Binary Robotics and Mechatronics. *IEEE/ASME Transactions on Mechatronics*, 17(5):857–865.

Haibin, Y., Cheng, K., Junfeng, L., and Guilin, Y. (2018). Modeling of grasping force for a soft robotic gripper with variable stiffness. *Mechanism and Machine Theory*, 128:254–274.

Henein, S. (2005). *Conception des structures articulées à guidages flexibles de haute précision*. PhD thesis, EPFL, Lausanne. Publisher: Lausanne, EPFL.

Henein, S., Bottinelli, S., and Clavel, R. (1998). Parallel spring stages with flexures of micrometric cross sections. In *Microrobotics and Microsystem Fabrication*, volume 3202, pages 209–220. International Society for Optics and Photonics.

Howell, L. L., Magleby, S. P., and Olsen, B. M., editors (2013). *Handbook of compliant mechanisms*. John Wiley & Sons, Inc, Chichester, West Sussex, United Kingdom ; Hoboken.

Huang, X., Kumar, K., Jawed, M. K., Nasab, A. M., Ye, Z., Shan, W., and Majidi, C. (2018). Chasing biomimetic locomotion speeds: Creating untethered soft robots with shape memory alloy actuators. *Science Robotics*, 3(25). Publisher: Science Robotics Section: Focus.

Ikuta, K. (1990). Micro/miniature shape memory alloy actuator. In , *IEEE International Conference on Robotics and Automation Proceedings*, pages 2156–2161 vol.3.

Ji, X., Liu, X., Cacucciolo, V., Imboden, M., Civet, Y., El Haitami, A., Cantin, S., Perriard, Y., and Shea, H. (2019). An autonomous untethered fast soft robotic insect driven by low-voltage dielectric elastomer actuators. *Science Robotics*, 4(37):eaaz6451.

Jin Qiu, Lang, J. H., and Slocum, A. H. (2004). A curved-beam bistable mechanism. *Journal of Microelectromechanical Systems*, 13(2):137–146.

Koh, J.-S. and Cho, K.-J. (2013). Omega-Shaped Inchworm-Inspired Crawling Robot With Large-Index-and-Pitch (LIP) SMA Spring Actuators. *IEEE/ASME Transactions on Mechatronics*, 18(2):419–429. Conference Name: IEEE/ASME Transactions on Mechatronics.

Kohl, M., Krevet, B., and Just, E. (2002). SMA microgripper system. *Sensors and Actuators A: Physical*, 97-98:646–652.

Kyung, J. H., Ko, B. G., Ha, Y. H., and Chung, G. J. (2008). Design of a microgripper for micromanipulation of microcomponents using SMA wires and flexible hinges. *Sensors and Actuators A: Physical*, 141(1):144–150.

Maffiodo, D., Raparelli, T., and Department of Mechanical and Aerospace Engineering, Politecnico di Torino (2017). Three-Fingered Gripper with Flexure Hinges Actuated by Shape Memory Alloy Wires. *International Journal of Automation Technology*, 11(3):355–360.

Must, I., Kaasik, F., Põldsalu, I., Mihkels, L., Johanson, U., Punning, A., and Aabloo, A. (2015). Ionic and Capacitive Artificial Muscle for Biomimetic Soft Robotics. *Advanced Engineering Materials*, 17(1):84–94. _eprint: https://onlinelibrary.wiley.com/doi/pdf/10.1002/adem.201400246.

Rubbert, L., Bitterli, R., Ferrier, N., Fifanski, S., Vardi, I., and Henein, S. (2016). Isotropic springs based on parallel flexure stages. *Precision Engineering*, 43:132–145.

Runciman, A., Xu, D., Pelton, A. R., and Ritchie, R. O. (2011). An equivalent strain/Coffin–Manson approach to multiaxial fatigue and life prediction in superelastic Nitinol medical devices. *Biomaterials*, 32(22):4987–4993.

Shyu, T. C., Damasceno, P. F., Dodd, P. M., Lamoureux, A., Xu, L., Shlian, M., Shtein, M., Glotzer, S. C., and Kotov, N. A. (2015). A kirigami approach to engineering elasticity in nanocomposites through patterned defects. *Nature Materials*, 14(8):785–789.

Sigmund, O. (2011). On the usefulness of non-gradient approaches in topology optimization. *Structural and Multidisciplinary Optimization*, 43(5):589–596.

Talischi, C., Paulino, G. H., Pereira, A., and Menezes, I. F. M. (2012). PolyTop: a Matlab implementation of a general topology optimization framework using unstructured polygonal finite element meshes. *Structural and Multidisciplinary Optimization*, 45(3):329–357.

Tolley, M. T., Shepherd, R. F., Mosadegh, B., Galloway, K. C., Wehner, M., Karpelson, M., Wood, R. J., and Whitesides, G. M. (2014). A Resilient, Untethered Soft Robot. *Soft Robotics*, 1(3):213–223. Publisher: Mary Ann Liebert, Inc., publishers.

Welsch, F., Kirsch, S.-M., Motzki, P., Schmidt, M., and Seelecke, S. (2018). Vacuum Gripper System Based on Bistable SMA Actuation. American Society of Mechanical Engineers Digital Collection.

Zhakypov, Z., Heremans, F., Billard, A., and Paik, J. (2018). An Origami-Inspired Reconfigurable Suction Gripper for Picking Objects With Variable Shape and Size. *IEEE Robotics and Automation Letters*, 3(4):2894–2901.

Zhang, H., Lerner, E., Cheng, B., and Zhao, J. (2020). Compliant Bistable Grippers Enable Passive Perching for Micro Aerial Vehicles. *IEEE/ASME Transactions on Mechatronics*, pages 1–1. Conference Name: IEEE/ASME Transactions on Mechatronics.

Zhang, X. M., Liu, A. Q., Lu, C., and Tang, D. Y. (2007). A Real Pivot Structure for MEMS Tunable Lasers. *Journal of Microelectromechanical Systems*, 16(2):269–278. Conference Name: Journal of Microelectromechanical Systems.

Zhu, B., Zhang, X., Zhang, H., Liang, J., Zang, H., Li, H., and Wang, R. (2020). Design of compliant mechanisms using continuum topology optimization: A review. *Mechanism and Machine Theory*, 143:103622.

Personal details:

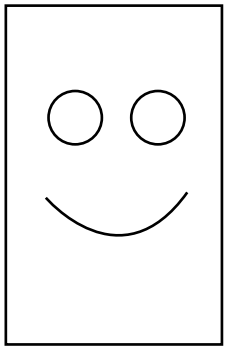

Name :	Mr. Sample CV
Address :	Samplestreet 70 6005 Luzern Switzerland
Date of Birth :	2nd of October 1981
Nationality :	Swiss
Legally work :	legally work in EU
Marital status :	with partner
Children :	none
Languages :	Chinese/Mandarin, English, French, German
Education level :	Bachelors degree
Hospitality work experience :	3-5 years
Special experience :	Europe work experience
Date of availability :	September 2009
Current location :	Africa
Travelling Status :	will be travelling single status
Telephone :	0041 41 370 6759
Email address :	jeff@h-g-r.com
Position(s) sought :	Permanent position for graduates
Department(s) sought :	Food & Beverage Bar/Sommelier

Personal profile:

As a Bachelor of Business Administration and after obtaining first relevant international work experience within the hospitality industry, I am now ready to take on new responsibilities to further my professional career.
My key strengths include strong analytical and logical skills, an eye for detail, communication and interpersonal skills.
I enjoy working in a team and help others progress. At the same time I work well independently.
As a highly motivated and driven individual I strive on taking up challenges.

Interests:

Travelling
Foreign Cultures
Photography
Sports

Educational qualifications:

Oct 99 - Feb 02	Higher Diploma (Hotel Management) Swiss Hotelmanagement School, SHL

Employment history:

Mar 04 - Ongoing	Assistant Manager (Rooms Division/Food & Beverage)
	Hotel Atlantic Kempinski Hamburg www.kempinski.com 5 star business hotel, part of Leading Hotels of the World 412 guest rooms, large function facilities, 3 food & beverage outlets
	Optimization of bar procedures, reinforcing SOPs
	Developing & implementing promotions
	Responsible for day-to-day operations
	Optimization and streamlining of housekeeping and laundry procedures
	Implementation of new SOPs
	Analyzing monthly reports for rooms division performance and sub departments
Mar 03 - Mar 04	Management Trainee
	Hospitality Graduate Recruitment www.h-g-r.com Leading company for placements within the Hospitality industry.
	Traineeship covering all aspects of an online recruitment agency.
Mar 02 - Mar 03	Management Trainee (Rooms Division)
	Hyatt Regency Xian, China www.hyatt.com 5 star business hotel 404 guest rooms, 4 food & beverage outlets
	Traineeship covering all rooms division departments on operational as well as supervisory level.

Training courses attended:

Mar 02 - Ongoing	OpenOffice - IT Courses
May 01 - Jan 03	Language Course - Chinese

References:

Hyatt Regency Xian
Patrick Sawiri, Phone: 86 22 2330 7654

Hospitality Graduate Recruitment
Jeff Ross, Phone: 41 41 370 99 88